

**Optimising the Parameters for Determining Alpha-Particle  
Energies from Digitised Output Waveforms From A  
Preamplifier Connected To A Silicon Detector**

PHYS841: Project Report for the MSc  
Radiometrics: Instrumentation and Modelling

Written by  
**Halil Furkan KIMKAK**

*Department of Physics*

Supervised by  
**Dr. Robert Page**

*Department of Physics*

Department of Physics  
The University of Liverpool  
United Kingdom  
September 25, 2020



## **Abstract**

In this project, it is aimed to detect and measure alpha radiation particles with hardware structure consisting of nuclear electronic components, pre-amplifier and analogue digital converter and consisting of silicon detector. Energy histograms have been obtained through digital signal processing including moving window deconvolution and trapezoidal filter techniques. The parameters giving the lowest FWHM value were compared in the histogram created by measuring the radiations of alpha particles emitted by Pu-239, Am-241 and Cu-244 radionuclides. During these studies, results were obtained by using software developed in an offline environment.

**Keywords:** *Alpha Radiation Detection and Measurement, Digital Signal Processing Algorithm, Moving Window Deconvolution Filter Parameter Optimization, Trapezoidal Filter Parameter Optimization, Alpha Spectroscopy with Silicon Detector and Nuclear Electronics, Energy Histogram Creation In Offline Environment*

## Acknowledgements

While high motivation and a lot of effort were made to complete this project (thesis), high motivation was provided, I support was given by many and I was always encouraged to do better.

First of all, my greatest thanks go to Dr Robert Page and Dr Andrew Boston for their continued support, guidance and critical advice during my master's education at Liverpool University and throughout this project work.

My thanks goes to Shiyamjith Nathaniel for his contribution to this work, the academicians and laboratory staff in the nuclear physics department at Liverpool University.

I would also like to express my gratitude to the Ministry of National Education, Republic of Turkey, for providing me with the opportunity to begin and pursue my MSc studies. All this scientific study was conducted with the support of the Republic of Turkey.

Last but not least, I would like to express my heartfelt gratitude to my family, my dear wife Büşra KIMKAK and my son for their support in keeping my motivation at the highest level in this excellent process.

Contents	
Abstract.....	i
Acknowledgements.....	ii
Declaration of Academic Integrity .....	v
List of Figures.....	vi
List of Tables.....	ix
CHAPTER 1: INTRODUCTION .....	1
CHAPTER 2: BACKGROUND AND THEORY .....	3
1.    Types of Radiation.....	4
1.1.    Alpha Radioactivity.....	6
1.1.1.    Radioactive Decay Law.....	8
2.    Semiconductor Detectors .....	10
2.1.    Silicon Detectors.....	11
2.2.    Heavy Charged Particles Detection.....	14
2.2.1.    Alpha Particles Detection .....	16
2.3.    Silicon Detector Instrumentation.....	18
2.3.1.    Vacuum Chamber .....	18
3.    Spectrum Analysis Criteria.....	19
3.1.    Resolution.....	19
CHAPTER 3: METHODOLOGY .....	23
1.    Energy Measurement.....	23
1.1.    Detector .....	24
1.2.    Charge Sensitive Preamplifier .....	24
1.2.1.    MesyTec Pre Amplifier (MPRT-16) .....	26
1.3.    ADC.....	28
1.3.1.    VHS-ADC .....	28
2.    Analogue Signal Processing .....	29
3.    Digital Signal Processing .....	30
3.1.    Comparison and Improvements of the Analogue and Digital Signal Processing Systems	
30	
3.2.    Advantages of Replacing Analogue Technology by Digital Software for Analysis .....	33
3.3.    Disadvantages of Replacing Analogue Technology by Digital .....	34
4.    MWD and Trapezoidal Filter .....	36
4.1.    Description of the Algorithm .....	36
CHAPTER 4: RESULT AND DISCUSSION.....	39
1.    Software Analysis.....	39
2.    MATLAB Programming Techniques .....	41
3.    Baseline Separation .....	41
4.    Time Constants Optimisation and Deconvolution .....	42
5.    Rising and Oscillation Part Extraction.....	47
6.    MWD Filter Histogram .....	48
7.    Trapezoidal Filter Parameter Optimization .....	50

8.	Histogram Creation.....	54
9.	Discussion.....	56
CHAPTER 5: CONCLUSION .....		58
FUTURE WORK .....		60
APPENDIXES.....		61
REFERENCES .....		72

## Declaration of Academic Integrity



### Declaration of Academic Integrity

NAME (Print)	<b>Halil Furkan KIMKAK</b>
STUDENT NUMBER	<b>201369801</b>
MODULE TITLE/CODE	<b>PROJECT/PHYS841</b>
TITLE OF WORK	<b>Optimising the Parameters for Determining Alpha-Particle Energies From Digitised Output Waveforms From A Preamplifier Connected To A Silicon Detector</b>

*This form should be completed by the student and appended to any piece of work that is submitted for summative assessment. Submission of the form by electronic means by a student constitutes their confirmation of the terms of the declaration.*

Students should familiarise themselves with Section 9 of the Code of Practice on Assessment and Appendix L of the University's Code of Practice on Assessment which provide the definitions of academic malpractice and the policies and procedures that apply to the investigation of alleged incidents.

Students found to have committed academic malpractice are liable to receive a mark of zero for the assessment or the module concerned. Unfair and dishonest academic practice will attract more severe penalties, including possible suspension or termination of studies.

#### **STUDENT DECLARATION**

I confirm that I have read and understood the University's Academic Integrity Policy.

I confirm that I have acted honestly, ethically and professionally in conduct leading to assessment for the programme of study.

I confirm that I have not copied material from another source nor committed plagiarism nor fabricated, falsified or embellished data when completing the attached piece of work.

I confirm that I have not copied material from another source, nor colluded with any other student in the preparation and production of this work.

SIGNATURE.....

DATE 25/09/2020

Halil Furkan KIMKAK

## List of Figures

- Figure 1. The electromagnetic spectrum radiant array with different frequencies and divided into different regions visually is shown. A very small fraction of this range is visible to the human eye (400 to 700 nanometres). Since at the bottom of this range is red light with a wavelength of about 800 nanometres, the part of the light spectrum just below this range is called infrared. Infrared light rays have a longer wavelength than visible light, so their energy is less. Microwaves and radio waves, on the other hand, have less frequency values than infrared light. .... 4
- Figure 2. Rn-222 is formed with the separation of the He atom from Ra-226, the first component. The  ${}^2\text{He}^4$  nuclei, consisting of two neutrons and protons, are alpha particles. .... 6
- Figure 3. The image to the left shows the formation of the ionization event. In the image on the right, the occurrence of the excitation event is shown. It affects the orbital electrons of the alpha particle passing near the atomic orbits. The picture on the left shows an electron breaking off its orbit (ionization). The image on the right shows the transition of an electron in the lower orbit to the upper orbit (excitation). .... 7
- Figure 4. The advance of the source emitting alpha particles in a collimator after the collimator leaves .... 7
- Figure 5. Graph representing Y-axis atomic number, X-axis representing neutron number. Due to the desire of radionuclides to stabilize, alpha and beta decays occur. The directions of the decays are shown in the yellow box above. As a result of the decays progressing in the direction of the arrows, radionuclides with different atomic numbers or neutron numbers are formed. .... 8
- Figure 6. Progress of alpha, beta and gamma photons in paper, aluminium and lead materials is shown. It is seen that the alpha particles shown at the top are completely absorbed by the paper. It is seen that the beta particles in the middle are absorbed by the aluminium by passing the paper. Gamma photons are not fully absorbed by both paper and aluminium. It appears to be completely absorbed by the lead. .... 9
- Figure 7. The energy band structure of semiconductor elements is shown. The green zone in the band gap indicates stateless energies. The blue zone includes energy states that are very heavily involved in the valence band. The conduction band, which is purple, indicates free states. .... 11
- Figure 8. The chemical bond structure of silicon and phosphorus elements is shown on the left. On the right, the donor level between the conduction and the valence band of an n-type semiconductor is shown. .... 12
- Figure 9. The chemical bond structure of silicon and boron elements is shown on the left. On the right, the acceptor level between conduction and valence band of a p-type semiconductor is shown. .... 12
- Figure 10. Chemical bond structure composed of silicon and boron elements. .... 13
- Figure 11. The structure shown in purple represents the valence band. The section shown in blue represents the conduction band. Valence band and conduction band are p-tip and n-tip, respectively. White small round shapes are holes and black small round shapes are electrons. Energy direction is shown on the left with a red arrow. .... 14
- Figure 12. The part shown with purple colour indicates the p type semiconductor type. The area painted in blue shows the n type of semiconductor type. The red and yellow regions in the middle indicate negative and positive ions. On the left side there are white small circular holes just next to the negative ions, while the small black circles next to the positive ions are electrons on the right. The red and yellow zone in the middle is defined as the depletion zone. .... 14
- Figure 13. High resolution spectrum obtained using surface barrier detector of Am-241 radioactive source [2, 9] .... 16
- Figure 14. Good resolution and poor resolution peaks are shown. The centre of both peaks is H<sub>0.20</sub>. .... 20
- Figure 15. It shows how good resolution and poor resolution peaks are seen when there are two. .... 20
- Figure 16. Graphical representation of energy resolution for detectors. Standard deviation is shown with sigma. Y indicates the maximum value of the peak. Y/2 is half the maximum value of peak 20
- Figure 17. The design set up to detect alpha particles using a silicon detector. The circuit element indicated by D is a diode. The alpha particle interacts with the silicon material and releases its energy to the detector, creating electron-hole pairs. A current signal is generated by the resulting pairs drifting in the electric field created by the high voltage. The voltage difference occurring during this time creates the pulse shown on the right of the figure. The area between the curve and the x-axis is directly proportional to the energy of the radioactive alpha particle [10]. .... 23
- Figure 18. Circuit diagram of a load sensitive preamplifier in a silicon detector (inside the square shown by the dashed line). High voltage is applied to the silicon detector. The resistor with 100 M

ohm value takes the majority of the current passing through the detector and pulls the high voltage on itself. In this way, the current passing through the detector is aimed to be at the lowest level. The circuit element shown with $C_1$ is a capacitor used to protect it from high voltage. The feedback contactor indicated by $C_f$ is induced with the negative side of the operational amplifier. The feedback resistance indicated by $R_f$ causes the capacitor to discharge.....	25
Figure 19. Plotted image of 5 microseconds pre-amplifier signal in MATLAB .....	26
Figure 20. This is the circuit diagram of the MPRT-16 product. The activated Input is the input of the signal from the detector for MPRT-16. There are 16 preamplifier outputs. There are two different timing filter out options. High voltage is fed to the circuit from the HV input shown at the bottom of the circuit diagram. Thanks to the 1 mega ohm resistor, a low voltage is provided for the rest of the circuit, because the 1 mega ohm resistor draws the majority of both the voltage and the current. There are triangular structures in the middle representing a charge sensitive preamplifier. Among these figures, it is seen that the gain polarity option is adjustable (Image taken from the ref. [14]).....	27
Figure 21. Image of MPRT-16 device using the signal from the silicon detector as input. In the image, 16-channel preamplifier output and 2 different timing filter out outputs are seen. In the section shown in blue, range and polarity are adjusted. In the Threshold section, voltages up to the specified value are prevented from passing. GND part is the cable entry place where the device is ground. The green led on the left represents that the circuit is powered, and the device is working. In the power section, high voltage input is made with a cable that can be tightened with a screw (Image taken from the Ref. [14]).....	27
Figure 22. Block diagram of VHS-ADC electronic device produced by Nutaq company. Picture taken from datasheet [15] provided by the company .....	28
Figure 23. An exemplary design of the system used until an alpha particle hits the detector and becomes a spectrum using analogue electronics. Within the rectangular shapes, the status of the signal is shown at each step. The pulse from the silicon detector is received by the preamplifier and generates a signal that is proportional to the energy of the ionizing alpha particle. Pulse amplitude is extracted with an ADC. It then turns into spectrum with an MCA.....	29
Figure 24. An exemplary design of the system used until an alpha particle hits the detector and becomes a spectrum using digital electronics. The signal output by the pre-amplifier is digitized by an analogue to digital converter. The pulse is converted into a spectrum directly through an algorithm whose amplitude is stored or processed in real-time.....	30
Figure 25. a) It is the signal form that outputs from the Preamplifier. Immediately after an alpha particle is detected on the silicon detector surface, a rapid rising edge and peak are formed. Then an exponential decay begins, determined by the constant $\tau$ of the voltage induced in the capacitor. b) The image of a flat top surface obtained by the deconvolution process of the signal that is exponentially decayed. c) The peak length is obtained as the window length determined by the M parameter used in the Moving Window Deconvolution filter. d) Trapezoid trapezoidal signal obtained by applying the L parameter used in the trapezoidal filter(Image was taken from Ref.[30]) .....	38
Figure 26. Display of parts of the trace obtained from the ADC output. Starting with the baseline, the trace starts rising with rise time and goes to the peak. Since some oscillation occurs due to noise such as cable transmission effects, there is an oscillation section. Next comes the exponential rising and exponential decay sections.....	40
Figure 27. No action trace. It is obtained from the ADC output.....	42
Figure 28. The signal obtained by subtracting the baseline mean from all data cells. The baseline level is on average zero.....	42
Figure 29. It is the section that increases exponentially after the oscillation section. The horizontal line shown in red is the end value of the exponential increase and the peak of the signal. The distance between the reference level and the signal datum is calculated.....	43
Figure 30. The total residual is obtained by summing the distance from the reference value. Time data are the time constant used in the exponential rise. The minimum point on the line chart corresponds to the lowest residual, where the corrected trace is closest to the reference line. ...	44
Figure 31. The signal after applying a correction to the exponential rising part.....	44
Figure 32. The distance between the red reference line and the trace is calculated for each datum. The red reference line is the peak of the signal at the defined starting point. ....	45
Figure 33. By using different time constants, the distance of the signal to the reference line is calculated each time the correction is applied. The distance with the least total distance to the	

reference line gives the optimum time value. The time axis shows the different time constants used for this analysis.....	45
Figure 34. A signal after applying the correction to the exponential decay part.....	46
Figure 35. The signal formed after applying corrections to both the exponential rising and exponential decay sections.....	46
Figure 36. Rising part and oscillation part have been removed. It is a trace consisting of a flat baseline and a flat proportional amplitude level. The adjusted trace has become a step signal....	47
Figure 37. Histogram consisting of 100 bars. The main peaks of radionuclides are shown in turquoise colour. Energy values of the main peaks are shown.....	48
Figure 38. Linear line equation and linear line created by the main peaks used for calibration...	49
Figure 39. Histogram shown with energy data. The energy values of radionuclides are specified. These energy values are calculated values. The parts shown in turquoise colour are the main peaks of radionuclides.....	49
Figure 40. The trace shown in orange is a step signal obtained by applying deconvolution of the signal from the ADC. The trace shown in blue is a pulse signal. For the trapezoidal filter, the signal has a width up to the desired point of use. The remaining data are discarded. The trace shown in purple is the trapezoidal filtered signal.....	50
Figure 41. Line graph obtained according to the changing flat top time values of FWHM (channel) data. It is shown for three different radionuclides. The line in green represents Pu-239, the line in blue represents Am-241, and the line in yellow represents the Cm-244 radionuclide.....	52
Figure 42. Line chart obtained according to changing rising time values of FWHM (channel) data. It is shown for three different radionuclides. The green line represents Pu-239, the blue line represents Am-241 and the yellow colour represents the Cm-244 radionuclide.....	53
Figure 43. Histogram created with a trapezoidal filter using the optimum flat top time and rising time parameters. It consists of 100 bars.....	54
Figure 44. Linear equation and linear line created according to the channel data of the peak of two main peaks .....	54
Figure 45. Histogram obtained with a trapezoidal filter and shown with energy data. The energy values of radionuclides are specified. These energy values are calculated values. The parts shown in turquoise colour are the main peaks of radionuclides.....	55
Figure 46. A spectrum consisting of Pu-239, Am-241 and Cm-244 main peaks (Provided from ref. [31].) .....	57
Figure 47. The change of the signal is shown for the moving window deconvolution filter and the trapezoidal filter. a) The trace shown at the top left is the digitized signal given by the Analogue Digital Converter and has not been added to any software yet. b) The trace shown at the top right is the signal obtained by subtracting the baseline level from the raw trace. The proportional amplitude value of the alpha energy is clearly seen as it is extracted from the baseline. c) It is the signal that is corrected after the optimum time constants for both exponential rising part and exponential decay part are determined. d) It is the step signal, which is the last step in the MWD filter. Unused parts have been discarded from the signal. The average of the high part of the signal directly gives the proportional amplitude value of the alpha particle. The histogram is the signal used to create. e) For the trapezoidal filter, the signal is clipped, and a pulse signal is formed. It determines the flat top time. e) It is the signal that occurs when the edges of the pulse signal become trapezoid after averaging in the window width determined for the formation of a trapezoidal filter. It is the last signal of the trapezoidal filter before the histogram is created.....	58

## List of Tables

Table 1. Classify tree according to ionizing and non-ionizing radiation types. Ionizing radiation also has sub-branches. These consist of two branches as direct and indirect. Alpha, beta, electrons, and protons build direct ionization, while photons and neutrons generate indirect radiation. ....	5
Table 2. Explanations of variables in the formula.....	17
Table 3. Data obtained using one of the strips in the Double-Sided Silicon Strip Detector. Each trace is 5 microseconds long, so there are 500 ADC data. In the data sets (11 rows) in each row of the table, the total number of recorded traces is written. ....	39
Table 4. Results of Moving Window Deconvolution filter obtained using OriginLab program. It shows the net area, FWHM, peak height and peak centre.....	48
Table 5. The calibration values used to switch from the Counts / Channel histogram to the Counts / Energy histogram. ....	49
Table 6. The data of Pu-239 peak are shown using the OriginLab Pro program. The flat top time value is varied while keeping the Rise time at a constant value. The FWHM, total peak area count, centre of the peak and height of the peak data are presented .....	51
Table 7. The data of Am-241 peak are shown using the OriginLab Pro program. The flat top time value is varied while keeping the Rise time at a constant value. The FWHM, total peak area count, centre of the peak and height of the peak data are presented. ....	51
Table 8. The data of Cm-244 peak are shown using the OriginLab Pro program. The flat top time value is varied while keeping the Rise time at a constant value. The FWHM, total peak area count, centre of the peak and height of the peak data are presented. ....	51
Table 9. The data of Pu-239 peak are shown using the OriginLab Pro program. The rise time value is varied while keeping the flat top time at a constant value. The FWHM, total peak area count, centre of the peak and height of the peak data are presented. ....	52
Table 10. The data of Am-241 peak are shown using the OriginLab Pro program. The rise time value is varied while keeping the flat top time at a constant value. The FWHM, total peak area count, centre of the peak and height of the peak data are presented. ....	53
Table 11. The data of Cm-244 peak are shown using the OriginLab Pro program. The rise time value is varied while keeping the flat top time at a constant value. The FWHM, total peak area count, centre of the peak and height of the peak data are presented. ....	53
Table 12. Table of values used to transform from histogram with channel data to histogram with energy data.....	54

# CHAPTER 1: INTRODUCTION

To measure the magnitude of the radiation, the detectors need to detect the radioactive particles. In this project, it is aimed to detect alpha particles and to create their energy histogram. In particular, the optimum parameters of some of the techniques used were investigated and compared to optimize the resolution.

A Double-Sided Silicon Strip Detector (DSSD), a type of semiconductor detector used in nuclear physics research, was used to detect alpha particles emitted from a standard calibration source. The DSSD was connected to MPRT-16 load sensitive resistor type preamplifiers produced by the MesyTec company. The preamplifier outputs were digitised by 14-bit VHS-ADC analogue-digital converters (ADCs) produced by the Nutaq company. All data were recorded and the whole analysis was done on offline platforms. The programming tool MATLAB was used to develop algorithms and software for the analysis.

Since each strip of the double-sided silicon strip detector is connected to a pre-amplifier and analogue-digital converter, each strip works like a silicon detector. Laboratory access has been restricted as the restrictions on education worldwide due to Covid-19 affect the educational processes in the UK. Therefore, previously recorded data from only one strip of a double-sided silicon strip detector was used. Therefore, the work has progressed according to the working principle and characteristic of a silicon detector. According to the results explained in more detail in the Result and Discussion section, there are only some minor differences in the energy histogram, but it does not affect the actual aim of the investigation.

In Chapter 2, detailed information is given about background and theory. Detailed information was given about the types of radiation and especially alpha particles, semiconductor detectors and especially silicon detectors, and finally the formulas and terms used in spectrum analysis.

In Chapter 3, methodology is included. In this section, nuclear electronic components, especially used in energy measurement, are explained. Pre-amplifier circuit structure is studied step by step. The working logic of analogue digital converter is emphasized. Next, analogue signal processing is briefly discussed. After detailed information on digital signal processing, there is a comparison with analogue signal processing. At the end of the chapter, technical information about the filtering techniques used, moving window deconvolution filter and trapezoidal filter, are explained.

In Chapter 4, the data set is processed using the techniques and theoretical approaches described in the previous chapters. For this purpose, first of all, all processes from the conversion of an alpha particle to a histogram energy are explained using software blocks encoded with MATLAB program. In the

meantime, optimum results were obtained for the time constants required for deconvolution. Additionally, optimum values of flat top time and rising time parameters used in the trapezoidal filter were determined. These determinations were made according to the Full Width at Half Maximum (FWHM) values.

Chapter 5 presents the conclusions of the project. In this section, the summary description of the study and its evaluation according to the results obtained are included.

## CHAPTER 2: BACKGROUND AND THEORY

Radiation can be defined as the energy transfer from one point to another in accordance with particle flow or wave theorem. There are many different types of radiation suitable for this definition. The primary classification criterion is whether this radiation occurs naturally in nature.

Some of the natural radiation comes from cosmic rays from space. Most of these rays are blocked trying to pass through the earth's atmosphere and only a very small amount reaches the earth's surface. Therefore, there is natural radiation affecting all living things in nature. The largest natural sources of radiation are stars, and the closest star to planet earth is the sun. That's why the biggest natural source of radiation is the sun. There are many natural radiation sources around the world. These are found in the atmosphere, soil, water, and rocks. Fossil fuels contain natural and long-lasting radioactive resources. There is no radiation hazard when such radioactive sources are in the fuel. But when they are burned and used, these radioactive elements travel towards the atmosphere. Then they return to the ground, causing a slight increase in the natural radiation level. One of the most critical reasons that increase the level of natural radiation is the radon gas released as a result of the decay of the radioactive Ra-226 source, which is common in the earth's crust.

To have high living standards in the industry, some radiation sources not found in nature cannot be sustained without using them. Therefore, according to the possibilities provided by technological developments, there has been a need to artificially produce some radiation sources. Artificial radiation sources cause exposure to certain amounts of radiation dose compared to natural radiation sources. However, the amount of radioactive exposure, depending on the amount, is much less than natural sources. It is an important feature that the possibility of the amount of dose exposed is low due to the complete control of artificial radiation sources. They are used in different fields including industry, medicine, research, military, and energy. These types of sources are artificial sources of radiation.

Another issue explained in this section is silicon detectors from semiconductor detectors. The physical and chemical structures of silicon detectors used for alpha spectrometry were studied. The changes that occur because of an alpha particle hitting the detector surface produced with the silicon element are explained. In this way, the first phase for the formation of a signal occurs. The interactions of a silicon detector with heavy charged particles are mentioned, and especially the detection of alpha particles is emphasized. The necessary parameters and formulas are given to evaluate the resolution in the histogram created with the energy of alpha particles.

## 1. Types of Radiation

There are two different types when classifying radiation sources. The first of these is divided into particle radiation and electromagnetic radiation. The other is the classification divided into two branches as ionizing and non-ionizing radiation.

If the first classification is taken into consideration, alpha particles, beta particles, heavy particles, subatomic particles, electrons, neutrons, protons can be given as examples of particle radiation. Alpha particles are high-speed helium nuclei consisting of 2 protons and 2 neutrons. Protons are positively charged particles with a mass of 1 atomic mass unit in atomic nuclei. Neutrons are particles with a mass of 1 atomic mass unit in atomic nuclei that do not have an electrical charge. Accelerated atomic nuclei are heavy particles, and subatomic particles are particles created by the breakdown of atomic nuclei. Electrons are negatively charged particles in atomic space. These are particles whose mass is much smaller than the proton and neutron. Beta particles are divided into two branches as negatron and positron. Neutrons are energetic electrons ejected from the nucleus because of radioactive decay and they are negatively charged. Positrons are the antimatter of the electron, and they are positively charged. Electromagnetic radiation, on the other hand, is emitted with photons in accordance with the wave nature in the electromagnetic spectrum (Figure 1).

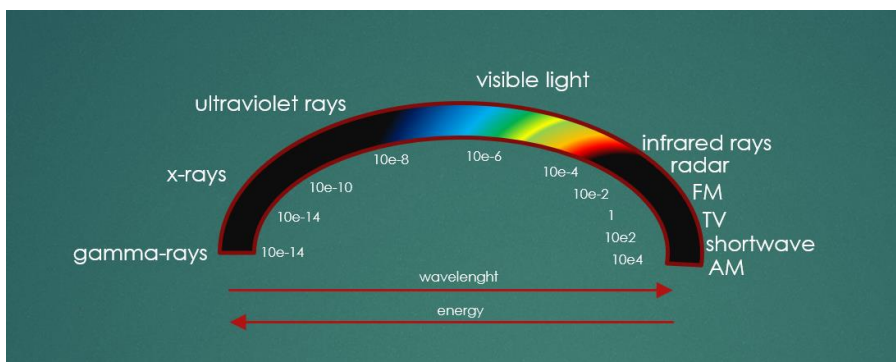
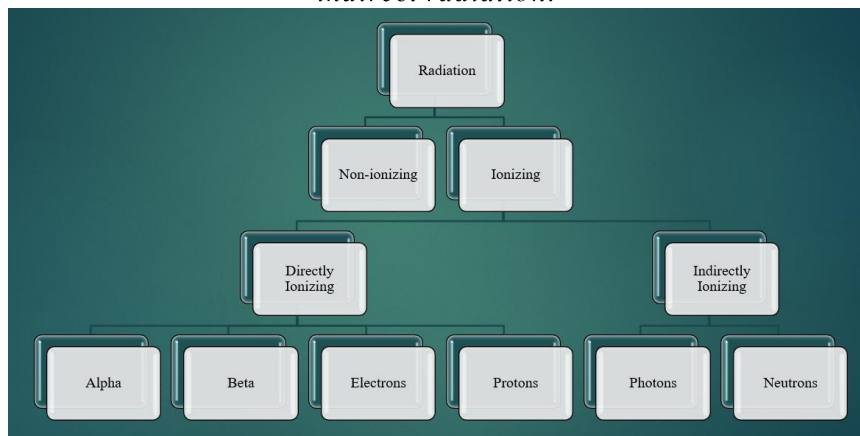


Figure 1. The electromagnetic spectrum radiant array with different frequencies and divided into different regions visually is shown. A very small fraction of this range is visible to the human eye (400 to 700 nanometres). Since at the bottom of this range is red light with a wavelength of about 800 nanometres, the part of the light spectrum just below this range is called infrared. Infrared light rays have a longer wavelength than visible light, so their energy is less. Microwaves and radio waves, on the other hand, have less frequency values than infrared light.

Another type of radiation classification mentioned above has two different subtitles as non-ionizing and ionizing radiation according to the interaction of radiation with matter, as seen in the Table 1. In ionizing radiation, they are those that can ionize an atom when its energy interacts with matter. This is not the case with non-ionizing radiation. As another explanation, the radiation particle, which has an energy above the energy value of an electron to be able to attach to an atom, can remove electrons from the atom. Therefore, such radiation causes ionization. Radiation with an energy lower than the energy

of an electron binding to an atom cannot ionize the atom. Hence, this condition is defined as non-ionizing radiation. All energetic electrically charged particles, alpha particles, beta particles, electrons, heavy particles and charged sub-particles are known as direct ionizing radiation, as seen in the Table 1. On the other hand, in the other branch, neutrons and protons have almost the same mass and are uncharged. By interacting with atomic nuclei, their range is longer than protons, and they indirectly ionize matter [1]. Gamma photons and X-rays, members of the energetic electromagnetic radiation family, are intrusive radiation. Therefore, they indirectly ionize the atom they interact with. Since all elements of electromagnetic radiation except X-rays and gamma photons do not have enough energy to ionize the atom, it is called non-ionizing radiation. Non-ionizing radiations that do not have enough energy to ionize the atom are infrared rays, ultraviolet rays, visible light, microwaves, and radio waves.

*Table 1. Classify tree according to ionizing and non-ionizing radiation types. Ionizing radiation also has sub-branches. These consist of two branches as direct and indirect. Alpha, beta, electrons, and protons build direct ionization, while photons and neutrons generate indirect radiation.*



### 1.1. Alpha Radioactivity

In 1896, Becquerel discovered radioactivity when uranium salts steamed photo plates. It was later discovered that there can be three different types of radiation. These were classified as alpha, beta, and gamma. It was found that alpha radiation is positively charged and effective at short distance. Alpha particles were captured in a glass tube filled with radon gas in 1907 by Royds and Rutherford. A discharge current was obtained using these particles. As a result of the investigations, it was noticed that the spectrum of helium matched with the spectrum obtained. It is known today that the  ${}_2\text{He}^4$  nucleus is alpha particles. Alpha particles consist of two neutrons and two protons (Figure 2). The alpha particles that are positive are a helium  ${}_2\text{He}^4$  nucleus and are symbolized by the  $\alpha$  sign.

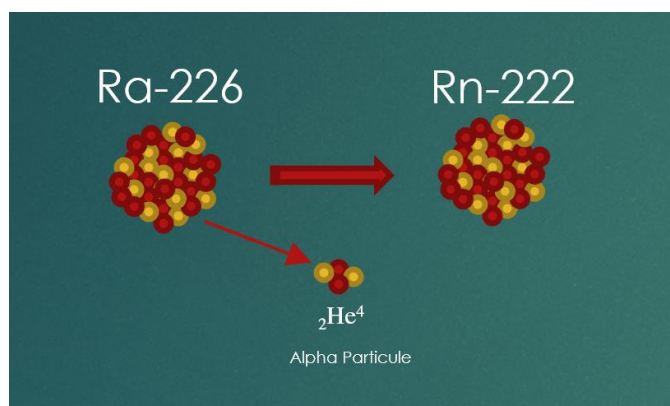
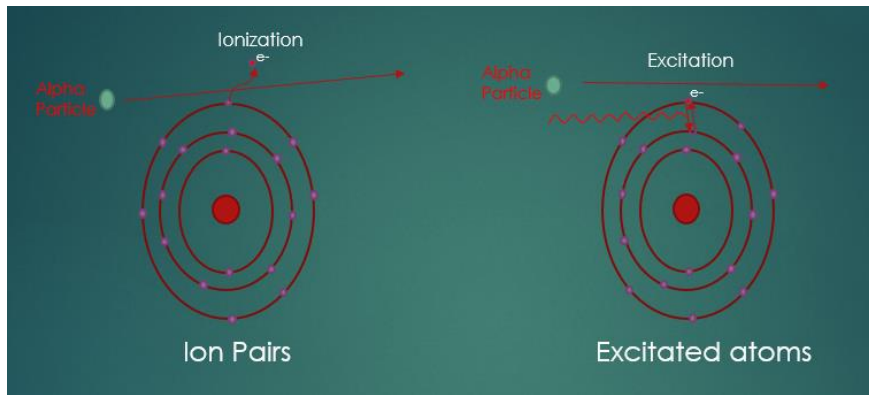


Figure 2. Rn-222 is formed with the separation of the He atom from Ra-226, the first component. The  ${}_2\text{He}^4$  nuclei, consisting of two neutrons and protons, are alpha particles.

On the other hand, alpha particles are formed or created in a number of different ways. These are;

- ❖ Some alpha-emitting nuclei are found in nature.
- ❖ Produced through nuclear reactors or as a result of nuclear explosions
- ❖ Production using some techniques in accelerator laboratories

After alpha particles enter the absorber atomic environment, interaction with electrons begins. Meanwhile, alpha particles feel an impulse as they pass around electrons. The reason for this impulse is magnetic caused by the coulomb force. The magnitude of the interaction varies according to the distance between the alpha particle and the electron. If the kinetic energy of the incoming alpha particles is greater than the bond energy of the electrons in the atomic space, it transfers enough energy to the electron and causes the electron to leave the atomic orbit. If the electron leaves its orbit completely, it is ionization, but if the electron rises to an upper orbital it is called excitation. The two different interaction events mentioned are shown in the Figure 3. Also, if the electron detached from the orbit through ionization, if it has sufficient kinetic energy, it creates more electron-ion pairs, which is called delta-ray production. Only delta-ray production and ionization are valid for detection in silicon detectors.



*Figure 3. The image to the left shows the formation of the ionization event. In the image on the right, the occurrence of the excitation event is shown. It affects the orbital electrons of the alpha particle passing near the atomic orbits. The picture on the left shows an electron breaking off its orbit (ionization). The image on the right shows the transition of an electron in the lower orbit to the upper orbit (excitation).*

As these kinds of electron and particle interactions continue, the speed of the particle constantly decreases. However, the alpha particles do not deviate significantly in the direction of such interactions, generally continuing to move linearly (Figure 4). Therefore, the progression of all charged particles, including alpha particles, through a substance is characterized by a certain range. Alpha particles emanating from an alpha source penetrate into a substance at the same distance.

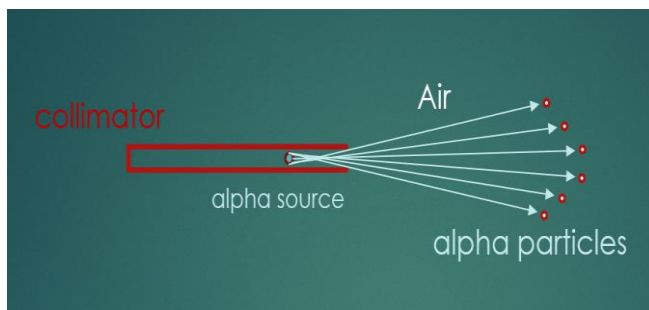


*Figure 4. The advance of the source emitting alpha particles in a collimator after the collimator leaves*

Ion pairs are defined as essential for the detector to detect. That is, one of the ion pairs consists of a free electron. The other is the positive ion created by the complete removal of the electron. Also, such ions tend to form a neutral atom.

### 1.1.1. Radioactive Decay Law

Alpha decay is governed by the law of radioactive decay, just like other radioactive decay processes. It is not known which of the atoms in a radionuclide sample will decay in any given time interval. All radioactive atoms in a sample have the probability of decay, and the decay equation for one of these atoms is shown in Equation 1.

$$N = N_0 e^{-\lambda t} \quad \text{Equation 2}$$

In this equation,  $t$  is time.  $N_0$  is the number of radioactive nuclei at the zero point in time.  $N$  indicates the number of radioactive nuclei remaining after the desired time to be calculated.  $\lambda$  is the decay constant and can be calculated with Equation 2 using half-life data.

$$\lambda = \frac{\ln 2}{t_{1/2}} \quad \text{Equation 3}$$

In the arrow directions indicated in the Figure 5, the stabilization of unstable nuclei is completed by alpha decays and beta decays.

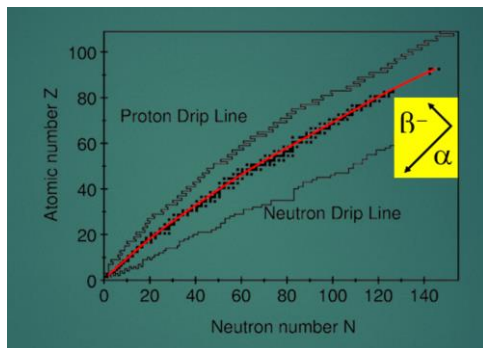


*Figure 5. Graph representing Y-axis atomic number, X-axis representing neutron number. Due to the desire of radionuclides to stabilize, alpha and beta decays occur. The directions of the decays are shown in the yellow box above. As a result of the decays progressing in the direction of the arrows, radionuclides with different atomic numbers or neutron numbers are formed.*

Detecting radiation begins with its interaction with the detector material. The Coulomb force occurs between the negative charge of the electrons in the absorber atom and the positive charge of the alpha particles. Through this force, alpha particles interact with matter. On the other hand, the interaction of alpha particles with the nucleus is very low in general. However, examples of such interactions are alpha-particle-induced reactions or Rutherford scattering. In the detector, which is responsible for detecting radiation, the interaction between the alpha particle and the atomic nucleus is not important enough. Therefore, the interaction with electrons in the detector material ensures that sufficient information about alpha radiation is obtained.

The destruction of the nucleus by extracting alpha occurs in natural radioactive sources. Also, atomic number occurs in large isotopes. As seen in the Figure 6, it is possible to intercept Alpha particles with materials of very short thickness. An example is a thin paper sheet. This is due to the large

electrical charges they have compared to other types of radiation. As alpha particles penetrate any substance, an intense ionisation occurs and thus causes their energy to decrease rapidly. Alpha particles, which lose their energy in this way, have very short travel distances to deeper. Therefore, there is no external radiation hazard in general. However, they can be dangerous when they enter the body through the stomach, respiratory tract and wounds, where internal radiation hazard may occur.

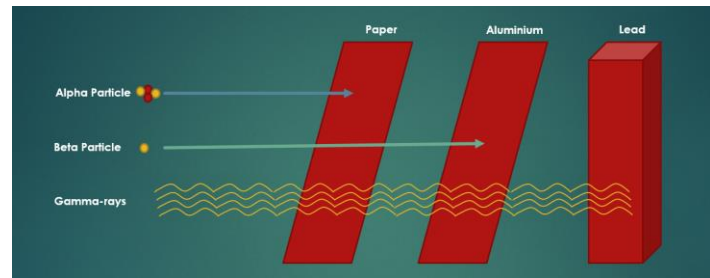


Figure 6. Progress of alpha, beta and gamma photons in paper, aluminium and lead materials is shown. It is seen that the alpha particles shown at the top are completely absorbed by the paper. It is seen that the beta particles in the middle are absorbed by the aluminium by passing the paper. Gamma photons are not fully absorbed by both paper and aluminium. It appears to be completely absorbed by the lead.

## 2. Semiconductor Detectors

Measurements are made by the interaction of nuclear radiation and atoms of matter. So primary ionization needs to be summed up. Density is among the most important criteria for two different elements to collide or one to affect the other. Therefore, solid materials used to detect radiation are more effective per unit distance in stopping radiation. Because solid substances are one thousand times higher in density than gaseous substances. In addition, semiconductor detectors offer the possibility to be designed in smaller sizes than gas-filled detectors. On the other hand, although scintillation detectors have a rigid detection structure, they offer relatively less resolution. The main reason for this is that the steps of converting the radiation into light, then amplifying it, and then generating an electrical signal lead to rather low efficiency. According to an explanation in the Knoll book, the energy resolution for 0.662 MeV is stated to be approximately 6% [2]. Also, due to a statistical limitation inherent in scintillation detectors, the resolution cannot be improved in any way. In summary, the statistical limit in radiation detection is a problem that leads to low resolution. The solution is to transmit with more carriers. This makes semiconductor detectors very advantageous in terms of resolution and size. In the first meeting of radiation and matter, the carriers in semiconductor detectors form electron-hole pairs. Additionally, electron-hole ion pairs formed in metal materials tend to associate rapidly. On the other hand, in insulators, the charge accumulation is almost non-existent at low voltage values. Therefore, semiconductor elements are widely preferred as radiation detectors. Metal materials and insulating materials are generally used for shielding radiation. Electron-hole pairs, which are similar to the ion pairs found in gas-filled detectors, generate the first electrical signal from the detector [2].

Semiconductor detectors, which started to be widely used in nuclear science in 1960, were first called crystal counters [3] and were based on the observation of ionization. They are then called solid-state detectors or semiconductor diode detectors. The working logic of modern semiconductor diode detectors is that they consist of junction diodes that pass current in only one direction. The incoming radiation causes ionization within the volume of the diode. As a result, it generates a current pulse that can be measured in the opposite direction to the normal current. Effective thickness, compact size and fast timing are known as advantages, while their low tolerance to radiation damage and the limitation of small dimensions are known as disadvantages. Germanium is often used to detect gamma photons in semiconductor detectors, which are commonly made of germanium and silicon. In this thesis, silicon detectors that provide more convenient detection for alpha particles and other charged particles will be discussed.

## 2.1. Silicon Detectors

Silicon element which has mass number 14 is commonly used in semiconductor detectors. This element has semi-filled outer electron shells. These crystalline elements contain four valence electrons in their final orbit. The atoms of these semiconductor elements, which tend to form covalent bonds, bond with their closest neighbours. Each atom in the Si crystal is connected to neighbouring electrons by four electron pairs. Electrons cannot move freely in the crystal. Therefore, pure silicone material is not a good conductor.

The energy levels of the valence electrons of the element silicon are very close to each other. For this reason, they form an almost continuous band of energy and this is called the valence band. As seen in the Figure 7, the pure state of the element silicon has a forbidden gap at the top of the valence band where there are no permitted energy levels. This band is called a forbidden gap and is approximately 1.115 eV [4] for silicon. There is a conduction band on top of the section called the forbidden gap. Electrons at this energy can move freely in the crystal and enable the conduction of electricity in the lattice. In other words, energy states are preserved between the conduction band and the valence band. These two bands are separated by a space called an energy gap. No energy flow is allowed in this range. Another characteristic of semiconductor elements is that it has a value between the voltage difference between the non-hollow conductors and the more hollow insulating elements, as seen in the Figure 7. Thanks to this feature, it creates a control mechanism related to the conductive properties of semiconductor elements. The energy levels of silicon valence electrons are very close to each other.

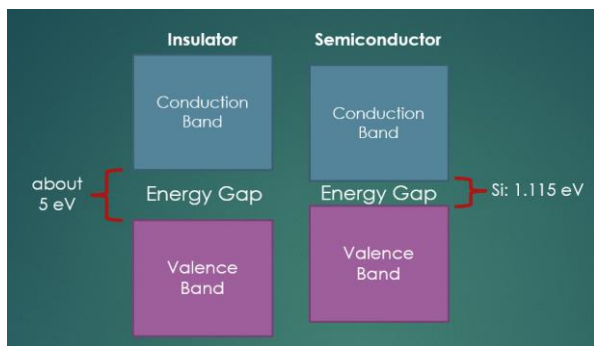


*Figure 7. The energy band structure of semiconductor elements is shown. The green zone in the band gap indicates stateless energies. The blue zone includes energy states that are very heavily involved in the valence band. The conduction band, which is purple, indicates free states.*

Crystals with impurity atoms in semiconductor detectors are called doped semiconductors. Those who have one extra valence electron in their impurity atoms are called donors. Impurity atoms with more valence electrons are called acceptors. While antimony, phosphorus and arsenic from the group V elements [5] are examples for donor, boron, gallium and indium [6] are sample elements for acceptor impurities. An excess of valence electron of the

donor element loosely bound to the crystal occupies the energy state near the conduction band region. Acceptor impurity elements, on the other hand, result in holes in the crystal due to missing electrons. The covalent bond is not strong and the energy state is induced in the energy gap range close to the valence band region [7].

As seen in the Figure 8, when one of the silicon atoms is replaced by a phosphorus atom, this impurity atom with five valence electrons forms four electron pairs with its neighbouring silicon atoms. Due to this bond, an electron is idle. This exposed electron is loosely bound to the phosphorus atom. It also contributes to the conduction of electricity in the crystal by breaking easily. Those with this type of property are called n-type crystals. Since an excess electron of phosphorus occupies a donor level very close to the conductivity band, it tends to easily rise to the conductivity band. Silicone containing Impurity is called n-type silicone; because the type that carries the charge within the crystal is negative.

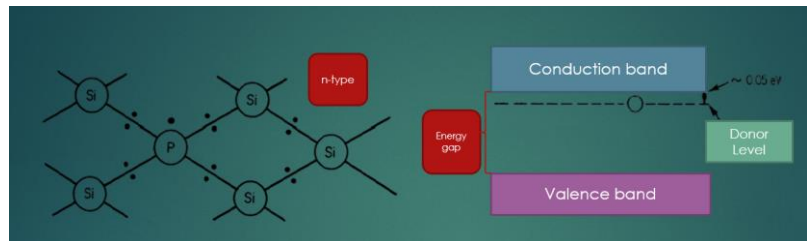


*Figure 8. The chemical bond structure of silicon and phosphorus elements is shown on the left. On the right, the donor level between the conduction and the valence band of an n-type semiconductor is shown.*

When one of the silicon atoms exchanges with a boron atom, this impurity atom with three valence electrons forms electron pairs with three neighbouring silicon atoms. An electron of a Si atom cannot form a pair. Therefore, a hole is formed in the silicon mesh as shown in the Figure 9. The lower occupies the acceptor level in a region very close to the valence band. That is, it can easily cross the valence band. Silicone containing impurity is called p-type silicon because the type that carries the charge in the crystal is positive.

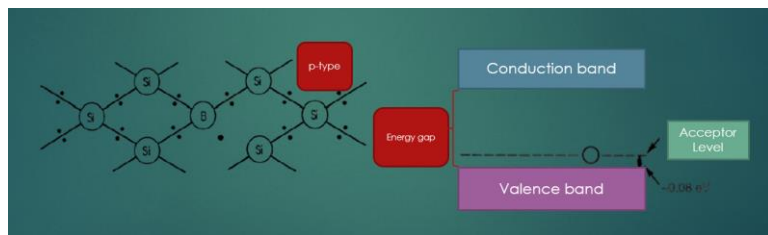


*Figure 9. The chemical bond structure of silicon and boron elements is shown on the left. On the right, the acceptor level between conduction and valence band of a p-type semiconductor is shown.*

A hole in the valence band is similar to an electron in the conductivity band and conducts electricity. Shown as Figure 10, the electron with number 1 moves towards the hole point indicated by the number 0 to fill the gap.

Therefore, a hole forms at the origin of the number 1 electron. Electron number 2 moves and moves forward to fill the hole made up of the number 1 electron. Similarly, the electron indicated by the number 2 creates a hole behind it. In general, when viewed carefully from the wide perspective, electrons move to the left, while holes move to the right. According to the definition of electricity, the movement of the charge conducts electricity. So, the movement of the hole from one place to another creates the flow of electricity.

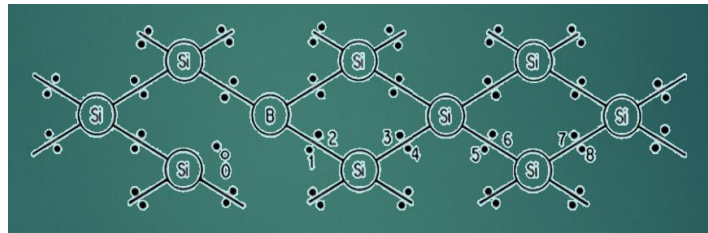


*Figure 10. Chemical bond structure composed of silicon and boron elements*

In summary, when enough acceptors or donor impurities are added to the silicon semiconductor element, either an n-type or p-type new structure emerges. As shown in the Figure 11 and Figure 12, the p-type and n-type are combined to form a semiconducting detector. In the resulting PN junction, the electrons that are surplus by the n-type material move towards the holes in the p-type material. An area is devoid of excess electrons and holes forms around the PN junction. This area is called the displacement (consumption) zone. This motion creates an electron flow. An electric field is induced to stop this current. Between both the p-type and the n-type side, the displacement region is now composed of inert loads attached to covalent bonds. The n-type side holds electrons, as well as the p-type side, holds the free charge carriers of the holes. The size of the depletion zone can be increased. This is possible with a reverse bias voltage applied at the junction. Thanks to the reverse bias voltage, the electrical voltage decreases on the p-type side. The electrons come to the p-type side and the holes to the n-type side. The bias voltage applied to the junction point is induced to block a current passing through the PN junction. Electrons move away from the joint due to the positive voltage in the N-type material. A thicker displacement zone is caused by the PN joint. The width of the displacement zone is directly proportional to both the resistivity of the silicon element and the square of the applied reverse voltage. The consumption of the displacement zone can be changed automatically by decreasing or increasing the voltage applied to the detector. Electron-hole pairs can be measured on the electrodes after the ionizing radiation has been labelled. The energy of the ionizing radioactive particle determines the number of electron-hole pairs created. As a result, this excitation and induction create an electrical pulse that is proportional to the energy of an alpha particle at the output of the device [7] [8].

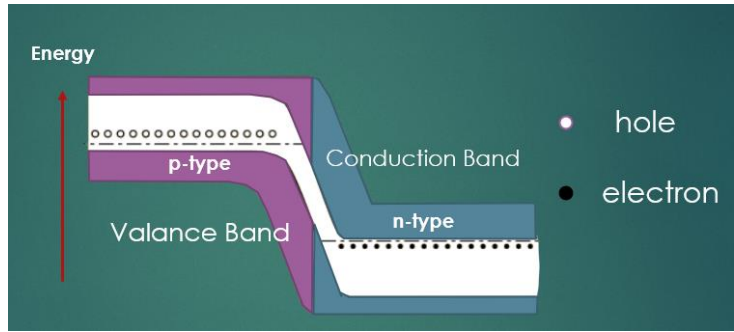


Figure 11. The structure shown in purple represents the valence band. The section shown in blue represents the conduction band. Valence band and conduction band are p-type and n-type, respectively. White small round shapes are holes and black small round shapes are electrons.

Energy direction is shown on the left with a red arrow.

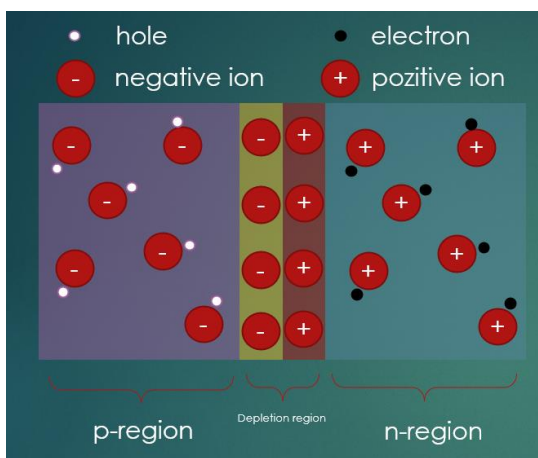


Figure 12. The part shown with purple colour indicates the p type semiconductor type. The area painted in blue shows the n type of semiconductor type. The red and yellow regions in the middle indicate negative and positive ions. On the left side there are white small circular holes just next to the negative ions, while the small black circles next to the positive ions are electrons on the right. The red and yellow zone in the middle is defined as the depletion zone.

## 2.2. Heavy Charged Particles Detection

Silicon diodes, which are semiconductor detectors that started to be used effectively in nuclear science thanks to the developments starting in 1960, are used to detect heavily charged particles. It is used in many fields such as energy losses of charged particles and spectroscopy of alpha particles. As fine and completely exhausted conduction detectors, fast electrons and beta particles are also used in silicon detectors. Compared to other detector types, it has advantages in terms of very good timing feature, high energy resolution, thin entry windows, relatively small size and ease of use [2].

Silicon diodes are commercially produced in dimensions of 20 cm wide and 20 cm long. However, the result of the corresponding large capacitance results in less resolution compared to small detectors. More general surface areas differ between  $1 \text{ cm}^2$  and  $5 \text{ cm}^2$ . Commercially produced depletion depths of up to 5 mm can be achieved in some specially prepared and designed configurations. Otherwise, detectors with more areas of use are limited to a depletion depth of 1 mm or less [2].

If the incident heavy ions are larger than the detector's depletion range, the detector's response is simple. This is because a single energy peak occurs for a single energy event particle. So there are no more complex processes such as partial energy accumulation or dispersal of the ion [2].

The depletion depth, which increases with test bias, is given with silicon wafer thickness only and only for fully depleted detectors. Thus, thanks to the prejudice applied to the detector, it can be used by ignoring the risk of failure in the detector. The maximum deviation value and the corresponding depletion depth is a feature specified by the manufacturer in the datasheet [2].

### 2.2.1. Alpha Particles Detection

Silicon semiconductor detectors are ideal detectors both for alpha particles and other light ions when operated at room temperature. Due to the widespread availability of monoenergetic sources suitable for alpha particles, the performance criterion of semiconductor type detectors offers the opportunity to test by recording the pulse height spectrum from such sources using old-fashioned methods. The most known of these is Am-241. The alpha spectrum corresponding to this radioactive element is often used in many places to compare the energy resolution of semiconductor detectors.

A spectrum taken with a silicon detector with a very high resolution value is presented in Figure 13 [2]. Alpha particles in the energy range of 5.486 MeV, the contribution of all electronic instrumentation including the preamp to the noise may be less than the energy resolution value of the detector. That is, it can be expected that the statistics of charge carrier generation will limit the energy resolution that can be obtained. This limiting resolution can be calculated using the Equation 6 below and Table 2 shows the explanations of variables in the formula.

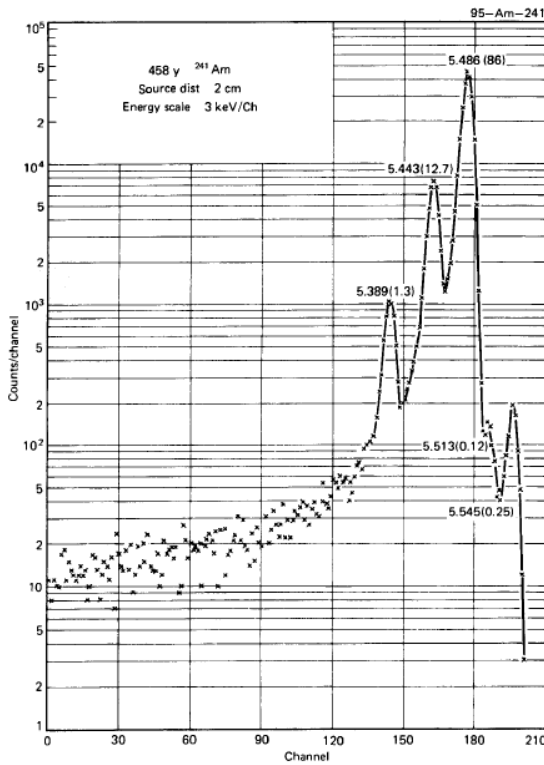


Figure 13. High resolution spectrum obtained using surface barrier detector of Am-241 radioactive source [2, 9]

$$R_{lim} = 2.35 \sqrt{\frac{F}{N}} = 2.35 \sqrt{\frac{F\epsilon}{E}} \quad \text{Equation 4}$$

*Table 2. Explanations of variables in the formula*

R	percentage energy resolution
F	Fano factor
N	average number of charge carriers / pulse
$\epsilon$	ionization energy
E	energy of the alpha particle

If the energy of alpha particles on both sides of the above equation is multiplied by (E), the following Equation 7 is obtained. Because in silicon detectors, instead of a resolution of energy, "full width half maximum value" is expressed in terms of energy units.

$$FWHM_{lim} = 2.35 \sqrt{F E \epsilon} \quad \text{Equation 5}$$

If it is calculated by giving some values for the variables in the formula ( $E = 3.62$  eV,  $F = 0.11$  and  $E = 5.486$  MeV), the "full width half maximum value" is 3.42 keV for the estimated statistical limit. For linear silicon detectors, an energy resolution of 8keV has been obtained for alpha particles. On the other hand, it has been observed that it is better than 10 keV in small size and commercially produced silicon detectors. Statistical inconsistencies affect the width of the peak in this type of detector. One of these statistical inconsistencies is because the energy of alpha particles is transferred to the recoil nuclei. Recoil nuclei at such low energies produce very few electron-hole pairs. If such losses were a stable value for all alpha particles, there would be no contribution or impact on the FWHM value. In addition, this loss of energy, which is affected by some larger events, is subject to large fluctuations. In silicon detectors such fluctuations are calculated as approximately 3.5 keV for 6 MeV alpha particles. Another reason for peak expansion is the effects of lack of collected charges and changes in energy lost by particles on the surface known as dead layer in silicon detector [2].

For detectors with lower energies and large capacitor values among charged particles, the noise originating from electronic components is also known as an important cause. The noise originating from the combination chosen for the amplifier and preamplifier can be suppressed for some reason. The first of these is the characteristic of the input level FET electronic component used in the preamplifier circuit. The second is the natural preamplifier noise and finally the fluctuations of the leakage current occurring in the detector. The noise originating from the combination chosen for the amplifier and preamplifier can be suppressed for some reason. The first of these is the characteristic of the input level FET electronic component used in the preamplifier circuit. The second is the natural preamplifier noise and finally the fluctuations of the leakage current occurring in the detector. In general, the sum of the squares of all FWHM values due to reasons contributing to the peak width can be summed up to equal the square of the final FWHM value of the detector.

### 2.3. Silicon Detector Instrumentation

The instrumentation methods used for silicon detectors have been the same for many years. However, there are vacuum chambers specifically for silicon detectors used in alpha spectrometry and electronics that come integrated with them. Such hardware is produced by being supported by software components.

#### 2.3.1. Vacuum Chamber

Although the band gap of silicon is 1.1 eV, visible light consists of photons with an energy of 2-3 eV. Therefore, a vacuum chamber was designed to prevent noise caused by visible light. In addition, silicon detectors are available in both vacuum and air-operated versions.

Some silicon detectors measure radioactive elements with a low amount of activity. Chamber cleaning is very important as there is always the possibility of material spillage from the source and backlash contamination. Some chamber materials are brass. Nickel coating is made on the brass. The chamber coating of some detectors can be in aluminium or steel. This is an advantage because it is very suitable for detailed cleaning in an ultrasonic environment.

Generally, the following qualifications must be provided.

- First of all, the chamber should be suitable for easy cleaning. The chamber becomes available for reuse after decontamination.
- The design between detector and source must be well defined and repeatable. An arrangement with gradual height adjustment is quite necessary. For example, a change of 0.1 mm is acceptable. In this way, the counting efficiency is the same for both the resources and the same for the standards.
- Alpha particles must reach the surface of the silicon detector without spending large amounts of energy. For this, the chamber should be operated at low pressure.

The things that need to be implemented and designed to produce a more useful silicon detector are as follows.

- The fact that the leakage current can be monitored by the person using the detector increases its usefulness for both calculation and tracking.
- For each chamber, the detector must have a security lock system that prevents the bias voltage until the air pressure decreases to a value lower than the desired level.
- There should be the option of applying a small bias voltage to the source holder to eliminate backlashes [9].

### 3. Spectrum Analysis Criteria

#### 3.1. Resolution

The main purpose of many applications applied in all other detectors such as silicon detectors is to measure the energy distribution of the radioactive particle coming to the detector. In other words, it is the most important factor in determining the energy of radiation. Resolution is simply the ability to distinguish between very close energies. In systems measuring radiation, the most critical feature of a silicon detector is the differential pulse height distribution generated by a detector, as seen in Figure 14, if the response of a radioactive particle to a monoenergetic source is examined. That is, resolution is measured by its response to single-energy radiation. While good resolution represents the response of a detector with high performance as shown in the figure, poor resolution can be said to be obtained from a detector operating with low performance. Assuming that the same number of radioactive particles are detected with both good resolution and bad resolution, the area between each peak and the x-axis is equal. Another point to note in both distributions is that although the average of both peaks is clustered around  $H_0$ , the widths of the peaks are different. While the width of the peak shown with good resolution is less, the width of the peak shown with poor resolution is larger. The difference in these width values proves that many pulsations from impact to impact are recorded, even if the same energy is detected in the detector for each radioactive interaction. If the number of such fluctuations is less, the corresponding peak width also gets smaller. Additionally, for better resolution, the peak tends towards a sharp increment or similar to the delta function. In other words, a sharp delta-function peak occurs in the ideal situation. Peaks are separated from each other in good resolution in a spectrum where two peaks are formed as seen in Figure 15. However, in the poor resolution curve, the two peaks are combined and cannot be distinguished. In the measurement of a radioactive source, the numerical specificity sensitivity in the incident energy of the radiation increases clearly as the width of the response function gets smaller. In reality, it is in Gaussian shape due to fluctuations in ionization. One of the reasons for the fluctuations is the drift of detector characteristics. Another reason is that there are random noises in the detector. Another reason for fluctuation is that statistical noise is caused by the fact that although the same energy is absorbed, it creates slightly different charge carriers. As a result, it is impossible to avoid fluctuations in the detector [2,9].

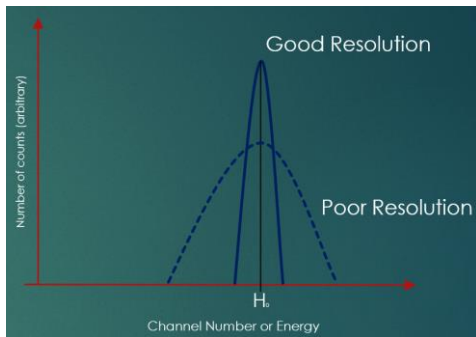


Figure 14. Good resolution and poor resolution peaks are shown. The centre of both peaks is  $H_0$ .

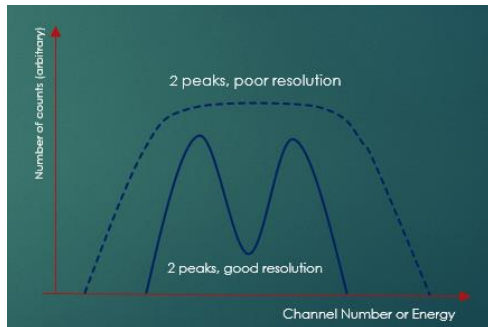


Figure 15. It shows how good resolution and poor resolution peaks are seen when there are two.

Energy resolution in radiation spectrometry is shown in Figure 16. The pulse height histogram for any detector is calculated according to the probability that the radiation is counted for the monoenergetic. The width of the half height (FWHM) is shown in Figure 16. It is the width that is half the maximum value of the hill on the y-axis. It is also assumed that any background noise that may occur above the maximum height of the peak is removed. The energy resolution of a detector is calculated by dividing the maximum value of full width half by the centre of gravity of  $H_0$ . Hence the energy resolution has a unit without dimension. Additionally, it is expressed as a percentage. Silicon detectors used to detect alpha particles have a detector energy resolution of less than 1%, while scintillation detectors used to detect gamma photons have an energy resolution value between 5% and 10%.

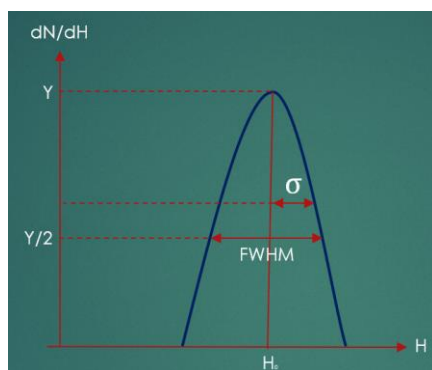


Figure 16. Graphical representation of energy resolution for detectors. Standard deviation is shown with sigma.  $Y$  indicates the maximum value of the peak.  $Y/2$  is half the maximum value of peak

When comparing the energy resolution of a detector, the smaller the number, the better the resolution. In other words, better separation of energy values that are close to each other is proportional to less resolution. When calculating energy solubilities, imperfect results are obtained due to some fluctuations. These unwanted fluctuations include the deviation due to the operation characteristics of the silicon detector during radiation measurements, random noise sources in the detector and the detector's instrumentation, and statistically defined noise caused by the signal itself measured in the alpha spectrometry.

No matter how flawless every part and part of the detector system is, the resulting signal has a slight fluctuation and therefore the third source is very important. In studies with large detectors, statistical noise is the source of fluctuation. Therefore, it creates a limiting limit on the detector's performance. The statistical noise that is the source of the fluctuation is due to the fact that the charge  $Q$  generated by alpha particles within the detector is not a continuous variable and represents a discrete amount of charge carriers. Ion pairs are formed when charged particles pass through the chamber in the ion chamber, and these are charge carriers. On the other hand, in scintillation detectors, the number of electrons collected in the photocathode gives the number of charge carriers. In both cases, although the number of carriers is different, the energy combined in the detector is the same. Despite this, different fluctuations occur from one radioactive event to another. The release of each of the charge carriers is an assumption Poisson process. In other words, the total average charge carrier produced is expected to have a standard deviation of the square root of the  $N$  number of charge carriers in order to describe the statistical fluctuations. If the statistical fluctuation alone influenced detector counting as a source of fluctuation, it would be expected that the monoenergetic peak in the spectrum would have a Gaussian shape. This is because the total average number of load carriers ( $N$ ) is quite large. Gaussian function is written according to Equation 16.

$$G(H) = \frac{A}{\sigma\sqrt{2\pi}} * e^{\left(-\frac{(H-H_0)^2}{2\sigma^2}\right)} \quad \text{Equation 6}$$

As shown in Figure 16,  $\sigma$  is the width parameter,  $H_0$  is the centre of gravity and  $A$  represents the area. As seen in Equation 17. Full Width Half is calculated with a maximum factor of 2.35 using  $\sigma$ .

$$FWHM = 2.35\sigma \quad \text{Equation 7}$$

Since the response is linear across detectors, the average amplitude ( $H_0$ ) of the pulse is calculated with Equation 18.

$$H_0 = KN \quad \text{Equation 8}$$

The parameter  $K$  in the formula is a proportional constant and  $N$  is the total average number of charge carriers. In this case, the width parameter  $\sigma$  is

calculated thanks to Equation 19. Equality is shown for FWHM in Equation 20.

$$\sigma = K\sqrt{N} \quad \text{Equation 9}$$

$$FWHM = 2.35 K\sqrt{N} \quad \text{Equation 10}$$

Using Equation 21 the resolution limited by Poisson is calculated.

$$R_{poissonLimit} = \frac{FWHM}{H_0} = \frac{2.35 K\sqrt{N}}{KN} = \frac{2.35}{\sqrt{N}} \quad \text{Equation 21}$$

As seen in the equation, the energy resolution limited by Poisson depends only on the N parameter, which is the total average number of charge carriers. That is, there is an inverse proportion between solubility and N (as N increases, R decreases). For better than 1% energy resolution, the total average number of charge carriers must be greater than 55000. Normally, a silicon detector has as many charge carriers per radioactive interaction as possible, so the limiting Poisson resolution R equals as few percent as possible. One of the biggest advantages of semiconductor detectors is that for each unit of energy lost by the detected radioactive particles, a fairly large amount of charge carrier is formed.

## CHAPTER 3: METHODOLOGY

### 1. Energy Measurement

A simple circuit diagram for detecting alpha particles with silicon detectors is shown in Figure 17. The high voltage applied to the silicon detector with semiconductor material shown by a diode symbol. This increases the volume of the depletion zone to the maximum volume. As mentioned in Silicon Detector section of Chapter 2, alpha particles enter the silicon detector and lose energy, forming electron-hole pairs. Due to the high voltage, charged particles drift, causing a current pulse to occur [10].

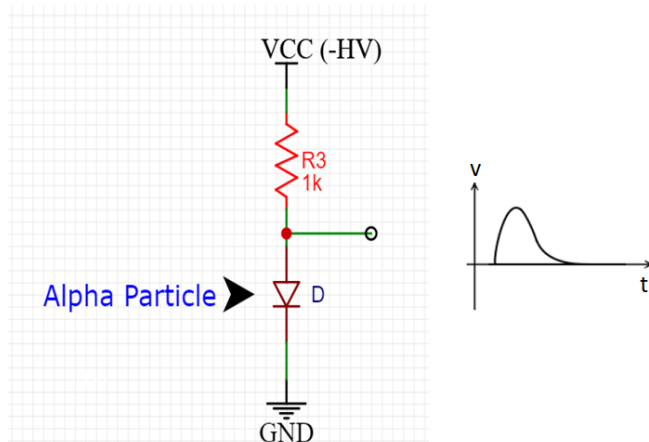


Figure 17. The design set up to detect alpha particles using a silicon detector. The circuit element indicated by D is a diode. The alpha particle interacts with the silicon material and releases its energy to the detector, creating electron-hole pairs. A current signal is generated by the resulting pairs drifting in the electric field created by the high voltage. The voltage difference occurring during this time creates the pulse shown on the right of the figure. The area between the curve and the x-axis is directly proportional to the energy of the radioactive alpha particle [10].

The alpha particle, which creates an interaction by hitting the silicon surface of the detector, causes some charge to be induced. This load energy is proportional to the amount of area under the current pulse curve. A charge sensitive preamplifier circuit is used to integrate the pulse signal into the electronic environment.

The signal generated by the integral is processed by a signal shaper before the total energy accumulated by the ionizing alpha particle is analysed by an analogue-digital converter and stored in the multi-channel analyser. Analogue-to-digital converters with fast sampling feature [11], also known as flash ADC, are developed using technological possibilities, the entire preamplifier output signal can be digitized. The energy stored in the MCA is extracted using a software coding either on the online platform or on the offline platform, e.g. moving window deconvolution.

### 1.1. Detector

The detector type used is semiconductor. A double-sided silicon strip detector (type BB20) manufactured by Micron semiconductor was used to collect data. The data obtained from only one strip of the detector with 192 strips were used. For more information, reference [12] can be reviewed.

### 1.2. Charge Sensitive Preamplifier

The preamplifier is the first electronic circuit element that connects to the detector and uses the signal from the silicon detector's instrumentation system. The purpose of using the preamplifier is to transmit the current signal to the rest of the circuit. Another task is to strengthen the signal. The preamplifier acts as a signal emitter to subsequent electronic circuit elements, modules, and other nuclear systems. The preamplifier circuit is kept as close as possible to the silicon detector. Because it is aimed to minimize the noise.

There are voltage sensitive, current sensitive and charge sensitive preamplifiers used for different applications. In spectroscopy using semiconductor silicon detectors, charge sensitive preamplifier circuits are normally used. A preamplifier circuit is shown in Figure 18. Generally, the preamplifier circuit is shown as an integrator. The feedback capacitor  $C_f$  is charged by the induced charge  $Q_d$  in the silicon detector. Consequently, an output voltage proportional to the induced load [10] is obtained from the preamplifier output. Before the preamplifier, a capacitor is provided to block the direct current high voltage component and only to transmit the current pulse as a result of the interaction by the radiation in the silicon detector [10]. In the ideally designed operational amplifier, the voltage difference between both gates is zero. Therefore, no current signal is input to the negative side [13]. Rather, current which comes from the silicon detector induces the feedback capacitor (Equation 22).

$$V_{C_f} = \frac{Q_d}{C_f} \quad \text{Equation 22}$$

After the short-term current pulse enters the preamplifier circuit, fast charging of the capacitor begins. After the capacitor is charged once, it is discharged by the operational amplifier in order to have equal voltage values on both of its gates. The current in the said capacitor is shown with Equation 23.

$$i_{C_f} = \frac{dQ}{dt} = \frac{dV_{C_f} C_f}{dt} = C_f \frac{dV_{C_f}}{dt} \quad \text{Equation 23}$$

Circuit elements in parallel have the same potential difference. Therefore, capacitor and feedback resistor have the same voltage value on both resistor and capacitor. Therefore, the current obtained from the output of the operational amplifier is shown in Equation 24.

$$i_A = \frac{V_{C_f}}{R_f} \quad \text{Equation 24}$$

According to Kirchhoff's law, the sum of all currents entering or leaving a junction is equal to zero [13]. Considering the junction point shown in Figure 18, there will be an equality as shown in Equation 25 and 26.

$$C_f \frac{dV_{C_f}}{dt} + \frac{V_{C_f}}{R_f} = 0 \quad \text{Equation 25}$$

$$V_{C_f}(t) = V_{C_f}(0)e^{-\frac{t}{\tau}} \quad \text{Equation 26}$$

In this case, output voltage will be as shown in Equation 27.

$$V_{out}(t) = -V_{C_f}(t) \quad \text{Equation 27}$$

The time constant used in the above equation is obtained by multiplying the  $R_f$  and  $C_f$  parameters. This time constant determines the curve that allows the instantaneous charge of the capacitor to decrease exponentially over time. Therefore, the pre-amplifier generates a decreasing voltage pulse with a maximum degree proportional to the induced charge due to the interaction of the alpha particle. The initial energy of the particle is proportional to the maximum tension of the pulse. Over time, the decrease continues exponentially up to the baseline level. Then these signals are sent to an ADC and digitized. As a result, pieces of information called traces occur.

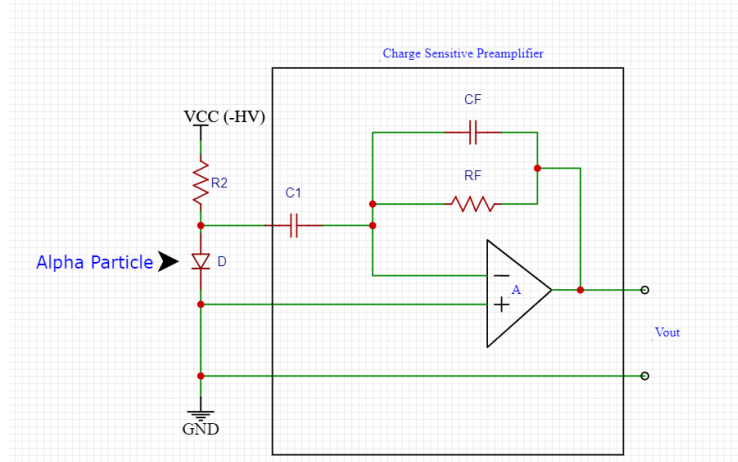


*Figure 18. Circuit diagram of a load sensitive preamplifier in a silicon detector (inside the square shown by the dashed line). High voltage is applied to the silicon detector. The resistor with 100 M ohm value takes the majority of the current passing through the detector and pulls the high voltage on itself. In this way, the current passing through the detector is aimed to be at the lowest level. The circuit element shown with  $C_1$  is a capacitor used to protect it from high voltage. The feedback contactor indicated by  $C_f$  is induced with the negative side of the operational amplifier. The feedback resistance indicated by  $R_f$  causes the capacitor to discharge.*

An example of trace is shown in Figure 19, with time on the x-axis time and the y-axis representing the proportional amount of the digitized voltage value

induced in the semiconductor detector by an ionizing particle. The signal from the preamplifier was digitized by a fast sampling analogue to digital converter (14-bit). By outputting the ADC with a clock time of 10 nanoseconds, traces of 5 microseconds were obtained from approximately 500 data.

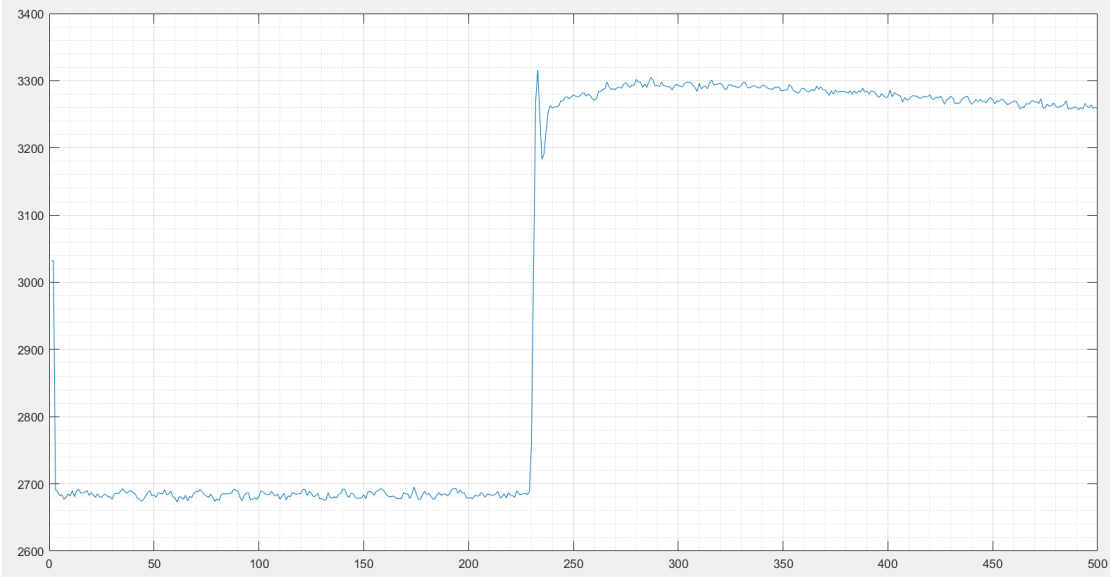


*Figure 19. Plotted image of 5 microseconds pre-amplifier signal in MATLAB*

#### 1.2.1. MesyTec Pre Amplifier (MPRT-16)

MPRT-16 preamplifiers supplied by the MesyTec company were used to obtain the traces analysed in this project. These multichannel preamplifiers were used because the silicon detector in this case was a double-sided silicon strip detector (DSSD).

According to the scheme shown in Figure 20, high voltage is connected to the circuit with 1 megaohm. The signal from the detector enters from the "Input" pin. Before the preamplifier, a 10 nano-farad sized capacitor is used. Thanks to the Input-protection, possible high voltage values are rejected in order to prevent damage to the integrated. Preamplifier output signal occurs according to gain polarity adjustment. There are 15 more inputs and preamplifier outputs like this.

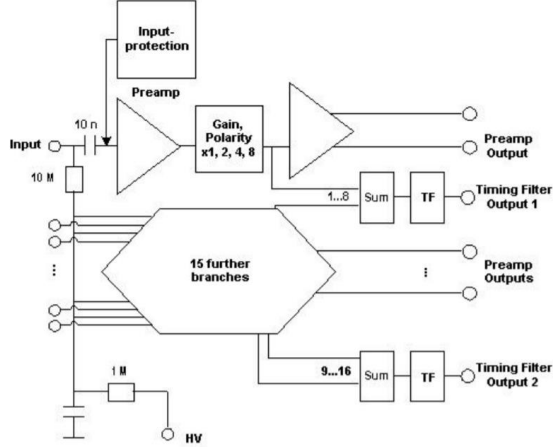


*Figure 20. This is the circuit diagram of the MPRT-16 product. The activated Input is the input of the signal from the detector for MPRT-16. There are 16 preamplifier outputs. There are two different timing filter out options. High voltage is fed to the circuit from the HV input shown at the bottom of the circuit diagram. Thanks to the 1 mega ohm resistor, a low voltage is provided for the rest of the circuit, because the 1 mega ohm resistor draws the majority of both the voltage and the current. There are triangular structures in the middle representing a charge sensitive preamplifier. Among these figures, it is seen that the gain polarity option is adjustable (Image taken from the ref. [14]).*

According to the MPRT-16 device shown Figure 21, the high voltage connector is connected in the power section. The output signal is taken from the 16-channel pre-amplifier output just above, via the locked flat connector cable. In the blue section on the side, range and polarity are adjusted with the help of a screwdriver. Two different cable inputs below left are used for timing filter out.



*Figure 21. Image of MPRT-16 device using the signal from the silicon detector as input. In the image, 16-channel preamplifier output and 2 different timing filter out outputs are seen. In the section shown in blue, range and polarity are adjusted. In the Threshold section, voltages up to the specified value are prevented from passing. GND part is the cable entry place where the device is ground. The green led on the left represents that the circuit is powered, and the device is working. In the power section, high voltage input is made with a cable that can be tightened with a screw (Image taken from the Ref. [14]).*

### 1.3. ADC

The trace exiting from the preamplifier section enters the ADC module in the next step. Here, the proportional voltage values of the shaped signals are digitized using an analogue to digital converter. There are different types of ADCs, but those with a peak sensing feature are preferred with load sensitive preamplifiers. There are also some different approaches in ADC peak detection techniques. The most common of these is the successive approximation technique.

#### 1.3.1. VHS-ADC

VHS ADC is a high-speed acquisition device manufactured by Nutaq company. It has Virtex-4 FPGA infrastructure to be used in high speed operations. As can be seen in the block diagram shown in Figure 22, it additionally has a maximum 105 MHz speed capacity and 8 simultaneous ADCs. Equipped with SDRAM for data storage, the VHS-ADC has 8 input and 8 output ports to store data at the same time. Baseband processing feature is used with the DC-coupled option. During the project, 14-bit resolution digitization capability was determined to work stably with other nuclear electronic components. For more information, reference [15] can be reviewed.

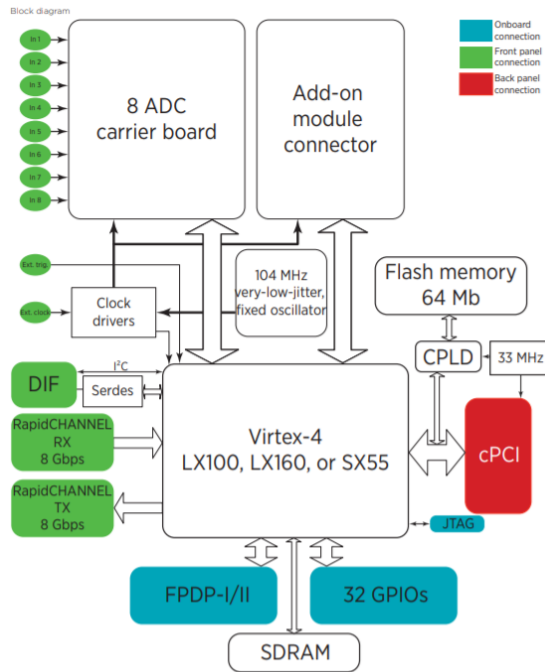


*Figure 22. Block diagram of VHS-ADC electronic device produced by Nutaq company.  
Picture taken from datasheet [15] provided by the company.*

## 2. Analogue Signal Processing

The analogue pulse processing setup, which consists of two different parts, shaping pulses and converting analogue data to digital, is shown in Figure 23. The pulse reaches a pulse shaper after passing a charge-sensitive pre-amplifier circuit. The pulse shaped here is very important because the exponential attenuation of the pulse output from the pre-amplifier circuit is theoretically infinite. Therefore, it is desired that the attenuation constant be as long as possible. Therefore, at any time, another alpha particle can reach the detector and generate a new pulse. Overlapping occurs when another signal arrives before a pulse decreases exponentially to the baseline level. Therefore, the proportional voltage value of the second pulse is added to the instantaneous weakened voltage value of the first pulse. So this means that the amount of stress created by the second impact will not be proportional to the charge of the second incoming alpha particle. To avoid this kind of problem, a gauss shaper is used. The shortening of the duration of the pulses and the long decay curves of the pulses are derived. Thanks to this technique, successive pulses are separated. In this way, the noise of the signal is reduced. Thanks to combinations of CR-differentiators, pulse shaping and RC-integrators with each other, analogue electronic installations are realized [2, 16].

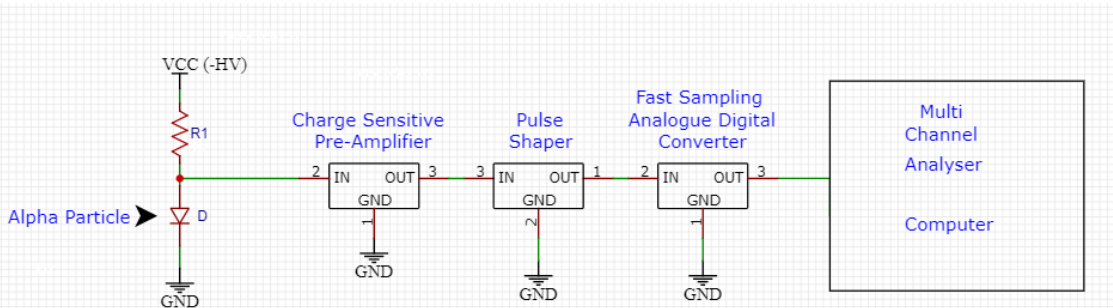


*Figure 23. An exemplary design of the system used until an alpha particle hits the detector and becomes a spectrum using analogue electronics. Within the rectangular shapes, the status of the signal is shown at each step. The pulse from the silicon detector is received by the preamplifier and generates a signal that is proportional to the energy of the ionizing alpha particle. Pulse amplitude is extracted with an ADC. It then turns into spectrum with an MCA.*

### 3. Digital Signal Processing

Thanks to the technology developed in 1990, fast sampling capability was developed for analogue-digital converters. As shown in the Figure 24, the trace from the preamplifier can be directly digitized. The time and amplitude of the pulses are now extracted using software algorithms. Depending on the purpose of the experiment or study, it can be analysed digitally online or offline. Digital pulse processing techniques provide a very flexible approach. In addition, signals are processed with less noise due to fewer electronic components. The most common method of separating the amplitude values of digitized preamplifier signals is MWD (Moving Window Deconvolution) mentioned in Section 4 [2].

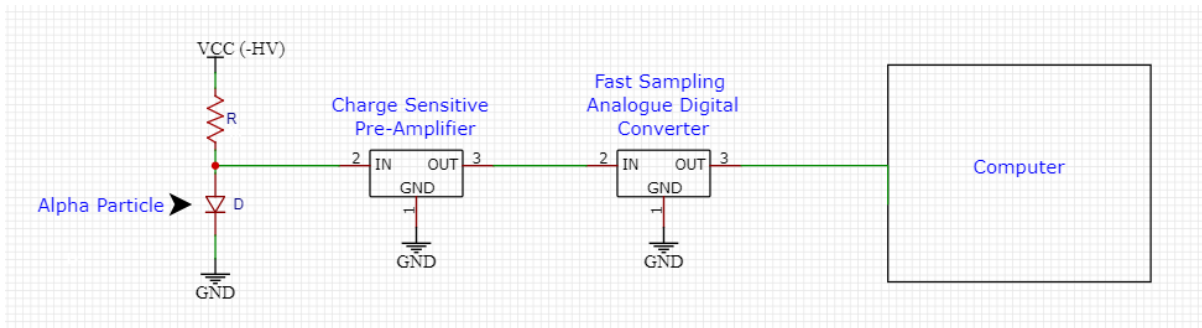


*Figure 24. An exemplary design of the system used until an alpha particle hits the detector and becomes a spectrum using digital electronics. The signal output by the pre-amplifier is digitized by an analogue to digital converter. The pulse is converted into a spectrum directly through an algorithm whose amplitude is stored or processed in real-time.*

#### 3.1. Comparison and Improvements of the Analogue and Digital Signal Processing Systems

The purpose of nuclear spectrometry studies is to produce digital signals that fully describe the properties, results and movements of radiation or interactions caused by radiation. In a nuclear spectrometry study, the energy of an alpha particle is absorbed in the silicon detector and converted into an electrical charge pulse, ready for measurement. In addition, apart from defining the energy of the alpha particle, the time of arrival at the silicon detector, its location, and the type of interaction can also be determined. During the passage of an electric current through any medium or matter, it may decay in different sizes as required by the laws of physics. In nuclear spectrometry, the current created due to the voltage difference created by the radioactive alpha particle coming to the sensing surface of the silicon detector becomes polluted with noise as the circuit progresses. However, the intensity, source and numerical modelling of the noise can be determined through the use of signal processing and electronic circuit elements. In addition, some filtering techniques, electronic circuit elements or software solutions are produced to be eliminated as much as possible. According to a theory called linear system, a filter with the best signal to noise ratio at the output of the circuit can be measured and proportional to the physical value [16]. While analogue signal processing techniques have been used for the best filtering

technique for a long time, digital signal processing techniques have been used frequently in the last decade. For example, Gaussian pulse shaping was used in analogue signal processing techniques. However, more current techniques and methods include field programmable gate arrays (FPGA), analogue-to-digital converters (ADC), and digital signal processors (DSP). In this way, a signal that has just emerged from the detector semiconductor material or a new signal from the new pre-amplifier electronic circuit can be digitally processed. In addition, thanks to the developing technological possibilities, real time work is carried out thanks to the circuit boards, circuit elements and software solutions with increased processing capacity. In a little more detail, simple and medium level operations of signal processing, triggering or reading operations are performed with FPGA circuit boards. DSPs can be used, added or increased for slightly more complex signal processing. Thanks to such technological opportunities, digital electronics have become a reasonable approach to signal processing, apart from the tasks of both data storage and control of the signal processing process. On this occasion, depending on the rapid advancement of technology, tools with high quality components are designed for each channel at affordable costs. Thanks to such tools and minicomputers produced for a specific task, pulse amplitude filtering, pulse separation, baseline restoration, pile-up correction and similar processes have been digitalized. Many standardized nuclear instrumentation modules (NIM), computer automatic measurement and control (CAMAC), VERSA-Module Europa (VME) and FAST BUS and similar modules have been developed using the very high performances of analogue to digital converter modules and FPGAs. In the early days, hundreds or even thousands of channels were designed from small-sized and small number of electronic circuit elements clusters, leading to the production of modules with higher benefits. While the first type designs, which are both low power consuming and compact, compromise performance, modules produced with newer techniques feature high performance. Digital signal processing techniques were first used in some theoretical studies in 1990 [17]. In such studies, its use in nuclear spectrometry was used for spectrometry of X-rays and gamma photons. As a result of these studies, the first patent was received in 1996. This patent was an independent external electronic device used in the gamma spectrometer used to analyse pulses from the pre-amplifier, which processes the signals from both the germanium detector and the silicon detector. With a few more companies doing similar studies, proprietary versions emerged. Later, DSPs were developed, packaged and released by many companies as an independent module. All such systems effectively combined the functions of the analogue digital convertor and amplifier. Some types even had the capacity to work with high voltage. Thanks to the advancement of technology, such studies have decreased to the capacity that smaller companies can do, and they have developed compact digital products that combine both the digital pulse processor and the preamplifier. All these

mentioned studies were compared in terms of differential accuracy, resolution, stability and efficiency [18] [19] [20] and it was found that they performed at the same level or higher than analogue systems. In other words, it has been observed that digital systems provide a very good solution in terms of both performance, efficiency and resolution compared to analogue systems. Many laboratories, including the Liverpool University Oliver Lodge Laboratory where this project was conducted, found it appropriate to use these digital components and instruments to perform nuclear spectrometry systems. It is aimed to develop higher efficiency, performance, resolution and similar features with the work carried out in this project and the studies carried out worldwide.

### 3.2. Advantages of Replacing Analogue Technology by Digital Software for Analysis

This section of the report describes the advantages of using digital technology in some aspects. Some of these are those.

- In terms of energy resolution, electrical signals are digitized earlier in digital systems. Therefore, both analogue components that need to be used to reduce the temperature problem and analogue components used for better resolution are used less.

- Higher resolution and less noise are obtained by using digital filtering techniques.

- Particles detected in nuclear spectrometry can arrive at any time. Therefore, there is no sequencing for the resulting signals. At the same time, the types of signals that come are not the same. When the number of alpha particles emitted by the radioactive material is high, a pile-up occurs in the detector. It is necessary to separate the overlapping signals, count the detected signals or reject the fewest possible signals to increase efficiency. Similarly, the pulse width of the incoming signal can be reduced in order not to reduce the efficiency, but it may adversely affect the energy resolution. Therefore, discarding digitally overlapping signals can affect efficiency more optimally.

- Digital types of nuclear spectrometry systems can be designed in small dimensions to use lower supply voltage and ease portability. Space, on the other hand, is advantageous in areas such as cultural heritage research or mining. In addition, due to the presence of an electronic device and equipment in laboratories, small size is advantageous for both cables and cases to take up less space. Devices manufactured and designed in the field of nuclear spectrometry can form large structures (such as accelerators) made up of small or small parts that can be used on a desktop. So, they are often technically complex and expensive.

- The structures used in electronically designed circuit boards consist of many logical structures. Generally, software is used in circuit elements made using electronic circuit elements such as the most important and most used transistor. Therefore, requests can be fulfilled via software without any soldering or adding any other circuit elements to the circuit board. In addition, illegal copying of digital systems due to reverse engineering is prevented.

- Some structures used in nuclear spectrometry systems need to be adapted for different detectors. When using analogue electronics, a variety of switch, screw or button positions that require operator expertise for critical adjustments must be adjusted. However, programmable logical structures provide great convenience when setting the most appropriate parameters in

digital spectrometry systems. Remote access or previously used programs can be saved to a hard disk and it is very easy to access from anywhere.

- Some structures used in digital spectroscopy systems can be planned to work multi-functional. For example, a configuration with multi-channel scaling, multi-channel analyser, or oscilloscope can only be created with some in-circuit programming.
- While filtering work, parameters determined in digital systems are not inconvenient to use the same parameters while working on another computer. Because it is guaranteed that the most optimal parameters working in one location do not change in another environment. However, the parameters created or used in analogue systems may change in time. This is because the electrical components become more sensitive over time and the structure is exposed to more vibration.
- Structures used in digital spectroscopy systems can be controlled simultaneously or at a scheduled time. In other words, if there is a leakage current at one point of the system, it is easy to detect as a result of software controls. Or it can be observed that the dc line is defective, the battery is low or there is a malfunction in the input / output structure of the pins of the microprocessor.
- Complete data acquisition and simultaneous tracking of incoming data is quite different in digital spectrometry systems compared to analogue spectrometry systems. Because the input signal is followed by a continuous clock signal, it is started and if it meets certain criteria, it is allowed to pass. Conventional analogue to digital converter systems have an event-oriented structure. However, in digital systems, an internal clock signal and time stamp are added for each information packet. There is a possibility of delayed reading. Incoming data is stored in an internal memory. It saves time and enables the spectrum to be efficient by processing the signals waiting in the memory of the processor in the first free time possible. Because the missed radioactive particle signals cannot be traced, you are not compared to analogue systems.

- Another advantage of digital systems over analogue systems is that the shaping parameters can be adapted according to the instantaneous signal flow. For example, for two successive particles, the forming constant of the first signal can be kept short in order not to miss the second signal. Thus, action can be taken for the signal coming in the second row. On the other hand, for a substantially isolated signal, the shaping time can be extended.

**3.3. Disadvantages of Replacing Analogue Technology by Digital**  
As well as the advantages of digital spectrometry, it still has some disadvantages from the people's point of view. Some of these are those.

- Due to the voltage difference that occurs when a radioactive particle hits the detector surface, the measured amplitude sensitivity depends on the sampling rate and the quantitation sensitivity. Generally, the process performed in an analogue digital converter occurs less quantification due to the higher sampling rate of the ADC.
- While some digital filters are used, such as the infinite impulse response, finite mathematical operations are used. Rounding errors occur during these operations. As a result, stability problems may occur.
- Special design skills are required to create digital integrated, module and electronic devices. Complex mathematical units, hardware identification and FPGA architecture are used using FPGA. Programs such as MATLAB and MATLAB Simulink are a bit more user-friendly and have drag-and-drop facilities. However, the cost of such programs is quite high, starting from \$ 10,000 per person. In addition, there are inconsistencies and differences in the products of companies selling DSP with the previous versions of the new versions they have developed.
- When the disadvantages of digital systems in terms of repair and maintenance are examined, a small change may not solve the problem, since most of the electronic components must be configured together. Therefore, in DSP systems with larger configuration settings, dealing with an incorrect point is not always the solution. In addition, due to the high complexity of DSP boards, the defective part is very difficult to detect. Such disadvantages result in high cost and time loss.
- There is very little extensive and non-formal training in digital spectrometry, with the exception of some manufacturers. Therefore, the number of people with sufficient expertise in spectrometer is small. Therefore, the number of open source platforms, software and hardware is very low. Since the interaction rate between people is less, the time spent for solving problems is more.

#### 4. MWD and Trapezoidal Filter

Some advantages of directly digitizing the signal output from the charge sensitive preamplifier circuit are mentioned in Section 1.2 of Chapter 3. The most suitable shaping for alpha radiation spectroscopy is the trapezoidal shape and cannot be achieved with analogue electronic methods. Half triangle and half gauss are generally used in analogue electronics. Another important advantage is that electronic components before the ADC, including ADC, are exposed to temperature changes and cause changes in the signal to noise ratio. Digital filters are not affected by temperature changes, but analogue filters are affected because of their physical structure. In addition, temperature changes are easily detected digitally and digital corrections are possible.

MWD (Moving Window Deconvolution) [21] [22] [23] is a mathematical algorithm used to calculate the energy of an alpha particle from the digitized charge signal. Moving Window Deconvolution basically consists of Moving Average (MA) and deconvolution stages. The first process in the MWD algorithm is to convert the exponential signal from the RC preamplifier into a step signal. In other words, it is done both before reaching the trapezoidal shape and removing the noise in the signal. The step signal is the output of a transistor zeroing amplifier.

When the studies in the literature are examined, it is seen that the MWD algorithm is not the only method for determining energy [24] [25] [26] [17] [27] [28] [29]. However, the moving window deconvolution algorithm is the most intuitive technique. Therefore, this algorithm has been studied and the results are presented in the following section.

##### 4.1. Description of the Algorithm

When a radiation is detected from the output of a charge sensitive preamplifier, a rapidly rising signal occurs due to load accumulation. The rise time of the signal in proportion to the radiation energy constitutes the final peak. Through exponential decay, there is a decrease in the signal's peak over time. The preamplifier effect is removed from the signal in order to make a quality and accurate ballistic measurement. For this, the moving window deconvolution algorithm is used.

First of all, all possible exponential decreases or increases are arranged so that the upper part of the signal is a flat surface. Ideally, the preamplifier output contains a single exponential decay. However, more than one exponential movement can be observed due to some noise (transmission of cables (ringing noise)) or components used in the circuit (FET / MOSFET).

From any point of the signal, the decay time, initial amplitude and start time of the signal can be accessed. Theoretically, assuming that there is only one exponential decay, if  $t_0=t=0$  is assumed as the starting point, the function  $f(t)$  is used as shown in Equation 28 and 29.

$$f(t) = Ae^{-\frac{t}{\tau}}, t \geq 0 \quad \text{Equation 28}$$

$$f(t) = 0, t < 0 \quad \text{Equation 29}$$

With the data of the amplitude  $f(t_n)$  at time  $t_n$ , the initial amplitude can be derived from the Equation 30, 31, 32 and 33.

$$A = f(t_n) + A - f(t_n) \quad \text{Equation 30}$$

$$A = f(t_n) + A \left(1 - e^{-\frac{t_n}{\tau}}\right) \quad \text{Equation 3111}$$

$$A = f(t_n) + \frac{1}{\tau} \int_0^{t_n} f(t) dt \quad \text{Equation 32}$$

$$A = f(t_n) + \frac{1}{\tau} \int_{-\infty}^{t_n} f(t) dt \quad \text{Equation 33}$$

For all calculations, it should be switched from continuous time form to discrete time form. This situation is achieved by using Equation 34 and 35.

$$A[n] = x[n] + \frac{1}{\tau} \sum_{k=-\infty}^{n-1} x[k] \quad \text{Equation 34}$$

$$A[n] = x[n] - \left(1 - \frac{1}{\tau}\right) x[n-1] + A[n-1] \quad \text{Equation 35}$$

Equation 7 and 8 generates the stair signal from the continuous discharge preamplifier signal. The information of pulse height is obtained by performing exponentially decreasing signal deconvolution.

When differentiation is applied to the form of the deconvolution equation shown in discrete time, Equation 36 and 37 are obtained.

$$MWD_M[n] = A[n] - A[n-M] \quad \text{Equation 36}$$

$$MWD_M[n] = x[n] - x[n-M] + \frac{1}{\tau} \sum_{k=n-M}^{n-1} x[k] \quad \text{Equation 37}$$

If the expressions in the formula above are arranged as in Equation 36 and 37, Equation 38, 39 and 40 are obtained.

$$D_M[n] = x[n] - x[n-M] \quad \text{Equation 38}$$

$$MA_M[n] = \sum_{k=n-M}^{n-1} x[k] \quad \text{Equation 39}$$

$$MWD_M[n] = D_M[n] + \frac{1}{\tau} MA_M[n] \quad \text{Equation 40}$$

The intended use of the moving window deconvolution algorithm is to convert the decay signal exponentially into a stepper function signal, rather than to a stair signal that is in an upward trend. The length of this function is  $M$ . The signal is deconvolutionized only within the  $M$  window. The delta noise contribution can be reduced by taking a moving average of length  $L$ .

A triangle is formed when the moving average length L and the window length M are equal, and a trapezoidal shape when the L parameter is less than the M parameter. The formula applied for the trapezoidal filter is Equation 41.

$$T_M^L[n] = MA_L MWD_M[n] \quad \text{Equation 41}$$

Since it is less than the L parameter, the difference gives the length of the flat top. Both sides of the trapezoidal shaped trapezoidal shape are L in length. Because the moving average operation starts before L in the signal length M with step function. The averaging process is completed after L. The image of the moving window deconvolution process is shown in Figure 25. After the flat top edge is obtained, the value of the trapezoidal filter gives the energy information. This is because the ballistic deficit problem has been compensated.

When there is a non-zero offset by the ADC, the trapezoidal filter is offset. Therefore, it is seen that the energy data is offset. When no alpha radiation is detected, the ADC receives a baseline level signal and the slope becomes zero trapezoidal.

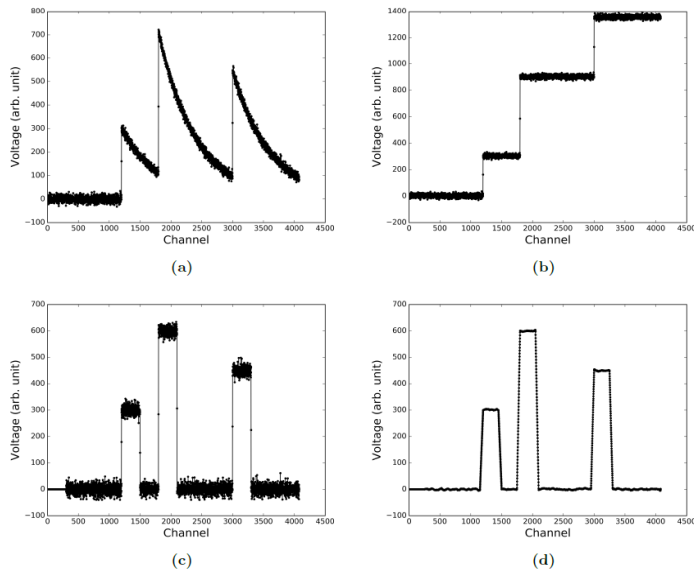


*Figure 25. a) It is the signal form that outputs from the Preamplifier. Immediately after an alpha particle is detected on the silicon detector surface, a rapid rising edge and peak are formed. Then an exponential decay begins, determined by the constant  $\tau$  of the voltage induced in the capacitor. b) The image of a flat top surface obtained by the deconvolution process of the signal that is exponentially decayed. c) The peak length is obtained as the window length determined by the M parameter used in the Moving Window Deconvolution filter. d) Trapezoid trapezoidal signal obtained by applying the L parameter used in the trapezoidal filter (Image was taken from Ref.[30])*

The optimum values of M, L and T parameters mentioned in this section have been investigated in Section 4, and 7 of Chapter 4 and the results obtained are presented. Additionally, MATLAB codes written to implement these algorithms are described in the next section and presented in APPENDIX 8.

## CHAPTER 4: RESULT AND DISCUSSION

This section primarily examines the structure of the data. Then, the results obtained with the techniques used in the MATLAB program are shown. Discussions were made with the determined values after parameter optimizations. There are results for two different filters. These are the moving window average (MWD) and trapezoidal filter (MA(MWD)). Time constants are specified for parameter optimizations, exponential rising part, and exponential decay part. Then, the flat top time and rising time parameters in the trapezoidal filter are determined. Counts/channel and counts/energy histograms were created according to the obtained optimum parameters.

### 1. Software Analysis

In this section, the MATLAB studies used for the digital use of trace data from the pre-amplifier are explained. Each trace contains 500 amplitude data. Each amplitude datum was recorded every 10 nanoseconds. That is, each trace is 5 microseconds long.

It has been digitized by a 14-bit ADC and transferred to the computer environment for offline operations. There are multiple ADC outputs, each recorded at different times. The column and row values of these data files are shown in Table 3. The row information shown in this table shows the number of different traces in the file. The number of columns shows the amount of data each trace has (10 nanoseconds each). The data were recorded from the strip number 32 of double-sided silicon strip detector. Each data file has been saved in Table 3 as in the name column respectively. The analysis was made with a total of 2460 traces. Data is imported into MATLAB as shown in Appendix 1.

*Table 3. Data obtained using one of the strips in the Double-Sided Silicon Strip Detector. Each trace is 5 microseconds long, so there are 500 ADC data. In the data sets (11 rows) in each row of the table, the total number of recorded traces is written.*

		Row	Column
1	DSSSD_R32strip_1	237	500
2	DSSSD_R32strip_2	238	500
3	DSSSD_R32strip_3	243	500
4	DSSSD_R32strip_4	254	500
5	DSSSD_R32strip_5	211	500
6	DSSSD_R32strip_6	236	500
7	DSSSD_R32strip_7	266	500
8	DSSSD_R32strip_8	235	500
9	DSSSD_R32strip_9	253	500
10	DSSSD_R32strip_10	213	500
11	DSSSD_R32strip_11	74	500

A trace that has not been processed is shown in Figure 26. When the figure is examined in detail, the part shown with the baseline is at the minimum level when the alpha particle is not detected by the detector surface. In other words,

when an alpha particle is detected, the rise starts from the baseline in proportion to the energy of the ionizing radiation. The "rise time" label, which should be noted in the figure, shows the time elapsed before the signal reaches its peak after the particle is detected. As can be seen in the preamplifier circuit design, the charging of the capacitor starts in this section. Since "ringing" noise occurs due to the signal transmission due to the cables, oscillation occurs just before the preamplifier signal reaches its peak. In addition, an increase begins exponentially. This problem is kept as low as possible by minimizing the transmission-induced noise. The signal, which continued to increase exponentially to its peak, was deconvolved using software techniques to obtain a flat peak. In Section 4 of Chapter 4, there is a detailed explanation about the optimum selection of the time constant depending on this increase. The pre-amplifier output signal, which reaches the peak level in proportion to the energy of the alpha particle, is expected to begin to decline exponentially. The process, which is expected to continue until the charge induced in the capacitor is discharged, is completed when the signal reaches the baseline level. However, since the recorded pre-amplifier signals are only 5 microseconds long, there is no exponential decay down to the baseline level. An exponential decay correction was applied in the recorded data to obtain a flat line, as explained in more detail in Section 7 of Chapter 4.

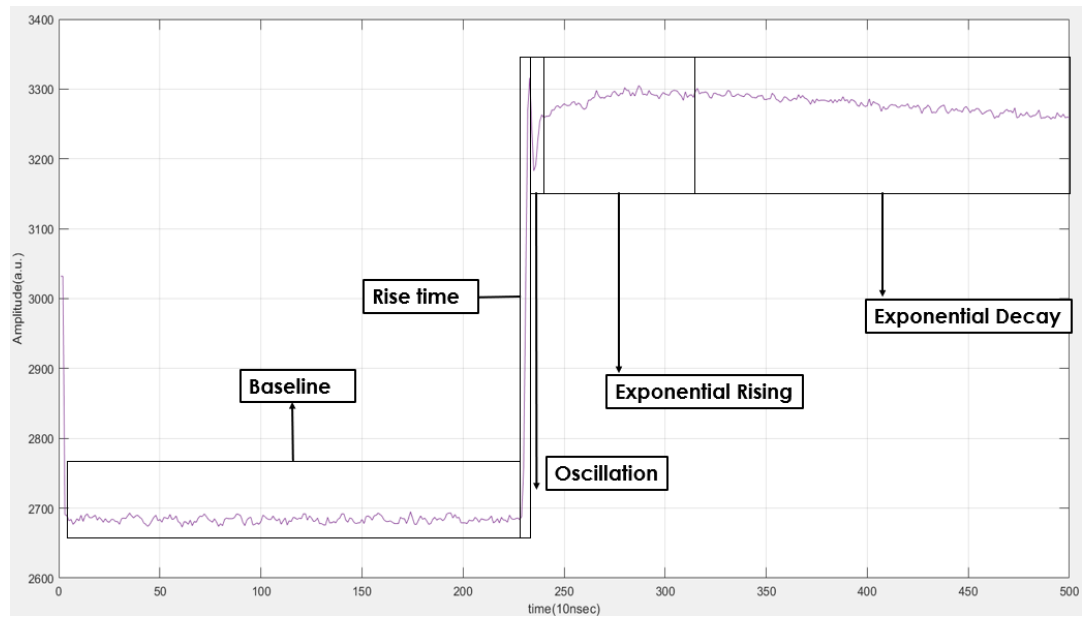


*Figure 26. Display of parts of the trace obtained from the ADC output. Starting with the baseline, the trace starts rising with rise time and goes to the peak. Since some oscillation occurs due to noise such as cable transmission effects, there is an oscillation section. Next comes the exponential rising and exponential decay sections.*

## 2. MATLAB Programming Techniques

MATLAB, named after the combination of the first syllables of the Matrix Laboratory words, was first published in 1985. It is a programming language developed by Moller. It is a product that can work interactively and efficiently, especially in a matrix-based mathematical environment. MATLAB, which is used in different areas today, has a wide range of products. It is defined as a highly successful language used in technical calculations [31]. Main usage areas of MATLAB include:

- Making applications with graphical user interface
- Conducting graphic-based studies in the field of science and engineering
- Conducting Monte Carlo studies in many fields, especially physics
- Modelling, prototyping and simulation studies

All MATLAB codes used in this project were created by the author. In general, "for" loop, "if-else" structures, and "switch-case" structures are used in all these codes. Variables and traces with preamplifier output are recorded in matrix a form. A different matrix space has been added for each file used. In other words, an 11-dimensional matrix was created with different row and column values of each preamplifier output consisting of 11 files (row X 500 X 11). Thus, a different matrix variable was determined in all steps and recorded step by step. The "plot" function was used to draw the graphs and the "hist" function for the histogram plotting [31].

## 3. Baseline Separation

In the signals obtained from the ADC output, the baseline remains constant at approximately one level due to the bias voltage. In direct proportion to the energy of the radiation, the signal rising up from the baseline level then begins to decrease exponentially. Since the difference between baseline and average peak level is proportional to the energy of the alpha particle, the baseline should be averaged. Therefore, the beginning and end parts must be determined. The baseline end time is determined with the algorithm prepared in the MATLAB environment. The baseline, which starts 30 nanoseconds after the signal starts to be collected, continues until the voltage drops when the alpha particle hits the detector. As seen in Appendix 2, the baseline end is determined if there is a difference of 70 units in the amplitude between the two data after 30 nanoseconds from the beginning of the signal. In other words, by calculating the 20 nanosecond differences, it is understood that the signal rises and the alpha particle interacts at the point where the difference is over 70. The baseline section obtained is averaged from the beginning to the end. This value is then subtracted from each datum of the trace. This will pull the baseline to approximately zero amplitude. In the remaining data, since the baseline voltage is subtracted, only the amplitude proportional to

the energy of the alpha particle remains. The remaining processes continue with these adjusted values. A trace is shown in Figure 27 before extracting the baseline. A trace with baseline averaged and subtracted from all data is shown in Figure 28.

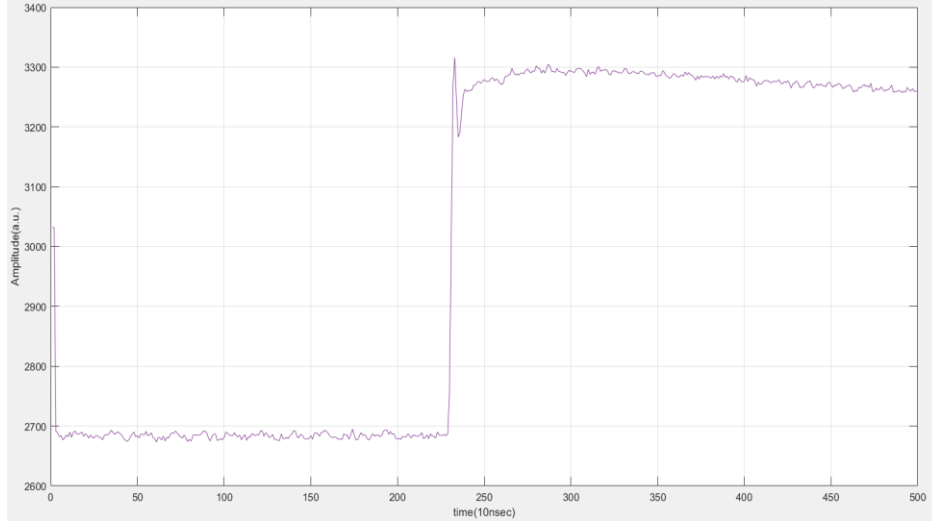


*Figure 27. No action trace. It is obtained from the ADC output.*

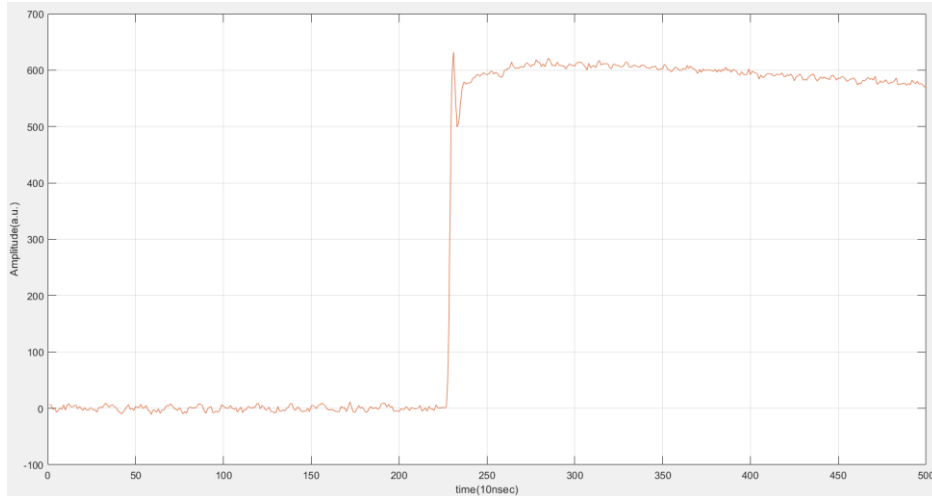


*Figure 28. The signal obtained by subtracting the baseline mean from all data cells. The baseline level is on average zero.*

#### 4. Time Constants Optimisation and Deconvolution

Two different time constant corrections have been made to make the upper section of the signal flat. The first of these is the moment when the alpha particle signal rises after being detected while in the trace baseline. After completing the signal increase, it oscillates to become resonance caused by cable transmission effects. This noise is called ringing [32]. The time constant of the exponential rise until the signal peak is determined. In this way, it is aimed to reduce the problem caused by noise as much as possible. The 275th datum of the trace was determined as the peak point, since it is accepted as the midpoint of both the exponential ascending part and the exponentially decreasing part. The starting time of the rising section is 120 nanoseconds

after the rise starting after the baseline level, because the oscillation part is completed after 12 data beyond the rising point. Since the 275th datum, which is the end of the rising exponential division, is considered as the maximum amplitude datum, the deconvolution equation has been applied for the data up to that time. As can be seen in Equation 41 and Figure 29, from the 275th datum ( $V_{t(0)}$ ) considered as the peak, the difference of the current datum ( $V_{t(i)}$ ) is taken and squared [33].

$$\text{Total Error } (k) = \sum_{i=1}^{i=n} (V_{t(0)} - V_{t(i)})^2 \quad \text{Equation 41}$$

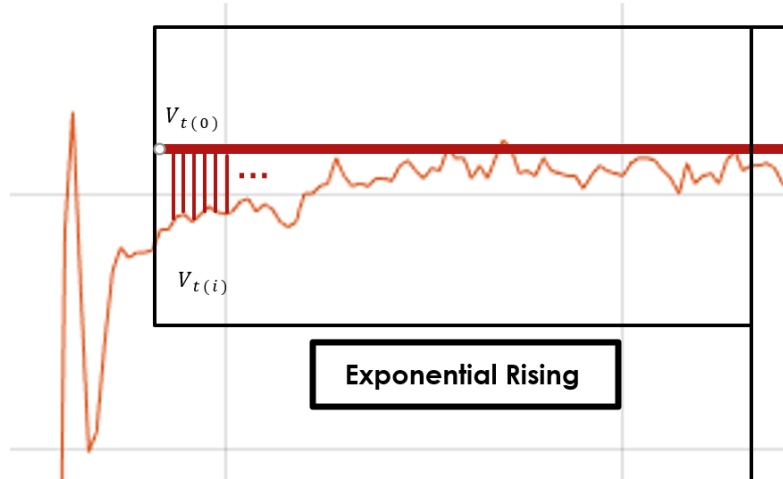


*Figure 29. It is the section that increases exponentially after the oscillation section. The horizontal line shown in red is the end value of the exponential increase and the peak of the signal. The distance between the reference level and the signal datum is calculated.*

In the section of exponential rising, the total margin of error was obtained by summing the squares of the distances to the optimum line. The time constant starts from 520 nanoseconds and continues up to 800 nanoseconds. The optimum time constant is the time to deconvolve the signal closest to the reference line. The graph of the results obtained with the software created to determine the optimum time constant is shown in Figure 30. That is, the minimum residual is the value at which the distance to the reference line is the least and the error is the least. When the graph is examined, the optimum time constant can be seen to occur at a value of 6.59 microseconds. When time constants greater than the determined optimum time constant are applied, the deconvolved signal rises above the reference line. Therefore, residual amount and error increase as the distances to the reference line increase again.

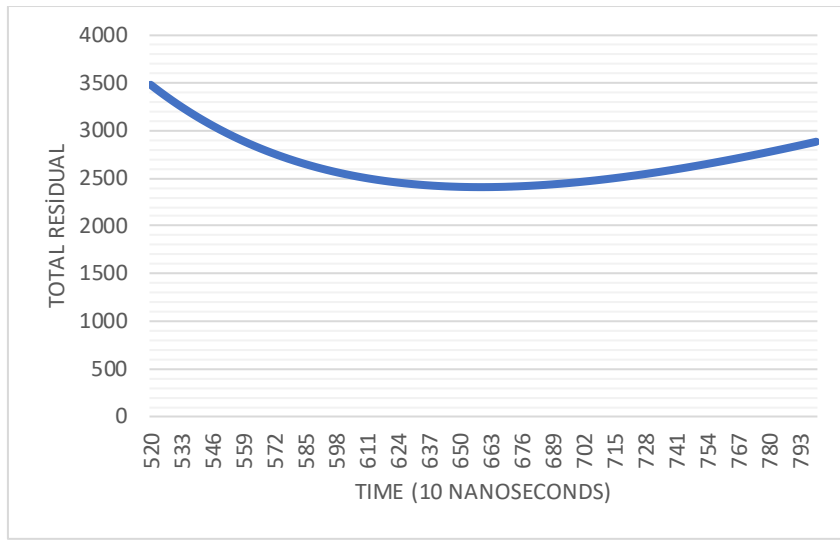


*Figure 30.* The total residual is obtained by summing the distance from the reference value. Time data are the time constant used in the exponential rise. The minimum point on the line chart corresponds to the lowest residual, where the corrected trace is closest to the reference line.

Using to the determined optimum time constant gives the adjusted signal shown in Figure 31. The signal shown in orange is an unprocessed signal. The signal shown in purple colour is the signal that has been deconvolved by using the optimum time constant determined only on the exponential rising segment. The prepared MATLAB algorithm can be examined from Appendix 3.

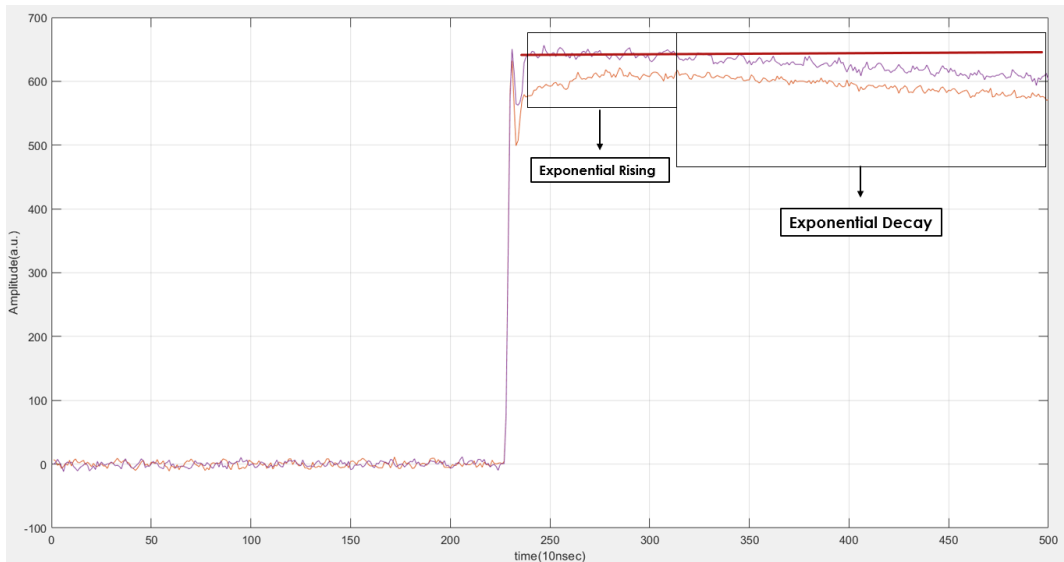


*Figure 31.* The signal after applying a correction to the exponential rising part.

For the exponential decay section the same method was applied as for the exponential rising section (Figure 32). In this way the optimum time constant has been found as 38.86 microseconds as seen in Figure 33. The time constant analysis was examined between 2500-5000 nanoseconds. At time constant values greater than the optimum time constant, the exponential decay section rises above the reference line. As the distance to the reference line increases,

the total residual begins to increase. The MATLAB algorithm prepared for optimization study can be found in Appendix 4.

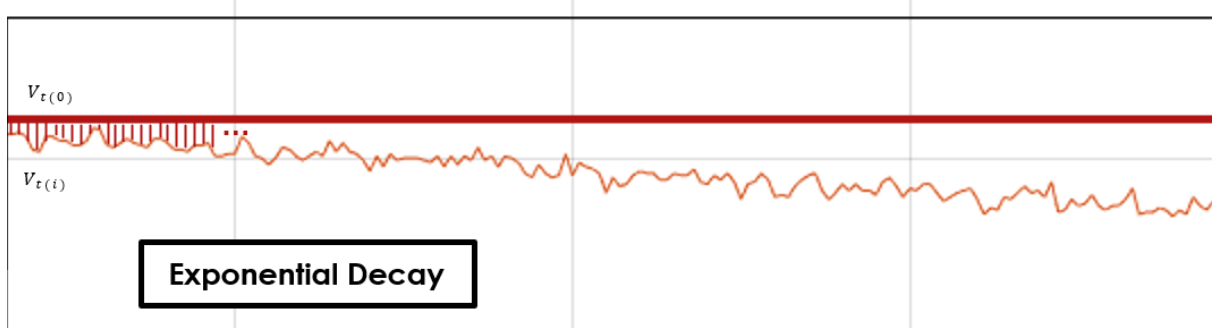


*Figure 32. The distance between the red reference line and the trace is calculated for each datum. The red reference line is the peak of the signal at the defined starting point.*

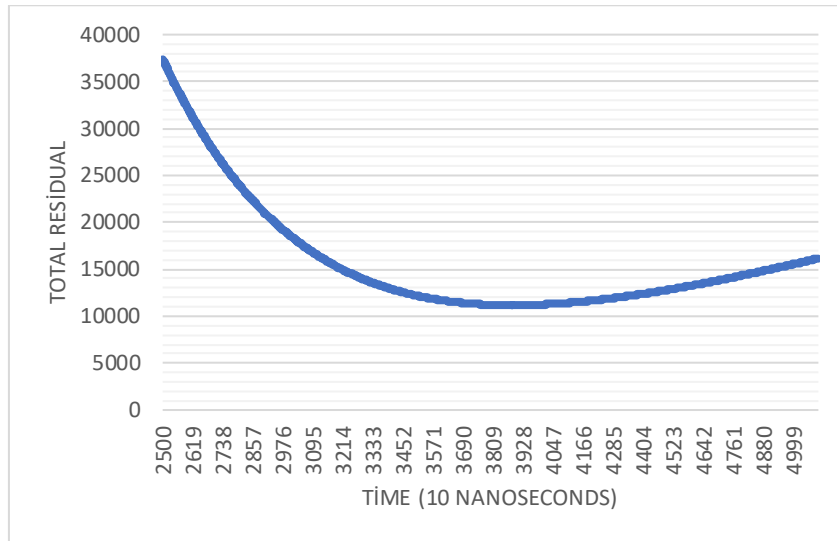


*Figure 33. By using different time constants, the distance of the signal to the reference line is calculated each time the correction is applied. The distance with the least total distance to the reference line gives the optimum time value. The time axis shows the different time constants used for this analysis.*

When the correction is applied according to the optimum time constant Moving window deconvolution method determined for exponential decay, the flattest possible signal is obtained as seen in Figure 34.

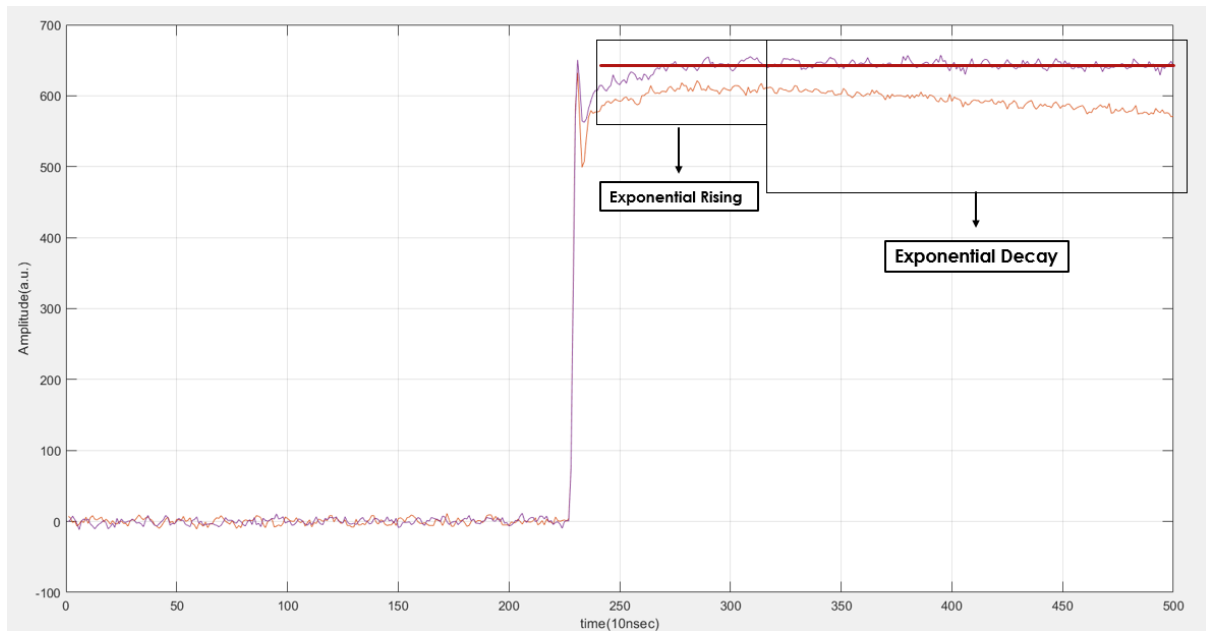


Figure 34. A signal after applying the correction to the exponential decay part.

When the results obtained for both exponential rising and exponential decay sections are combined, the signal shown in Figure 35 is obtained. The prepared MATLAB algorithm can be examined from Appendix 5.

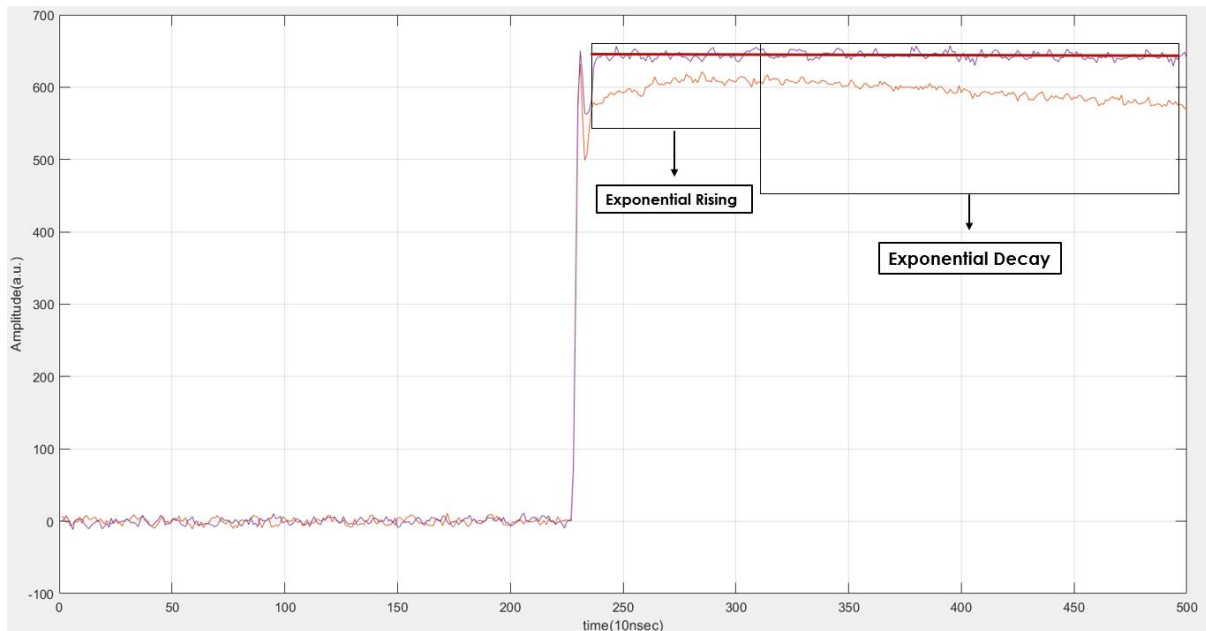
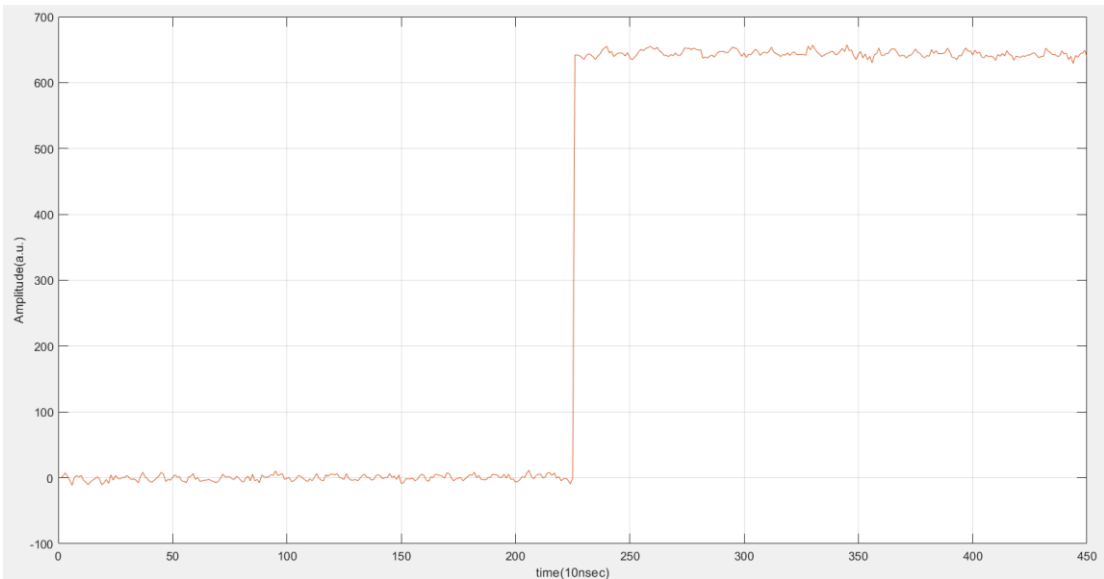


Figure 35. The signal formed after applying corrections to both the exponential rising and exponential decay sections

## 5. Rising and Oscillation Part Extraction

After applying all the above corrections, the baseline average is at zero level and stable, while the exponential increasing and decreasing segments give a flat level. With the removal of the rising and oscillation sections between these two sections, it is possible to work with fewer data and more optimum results are obtained while taking an average. Therefore, by determining the baseline end time, the beginning of the ascending segment is known. The ending of the oscillation episode is 120 nanoseconds after the beginning of the rising part. As a result of removing the specified parts from the signal (codes can be examined from Appendix 6), the signal seen in Figure 36 is obtained.



*Figure 36. Rising part and oscillation part have been removed. It is a trace consisting of a flat baseline and a flat proportional amplitude level. The adjusted trace has become a step signal.*

## 6. MWD Filter Histogram

The proportional amplitude values obtained by taking the baseline average and the flat top average were used to create the histogram. The signal type specified in Section 4 of Chapter 4 was applied for all data and a histogram with a total number of 2460 counts was obtained.

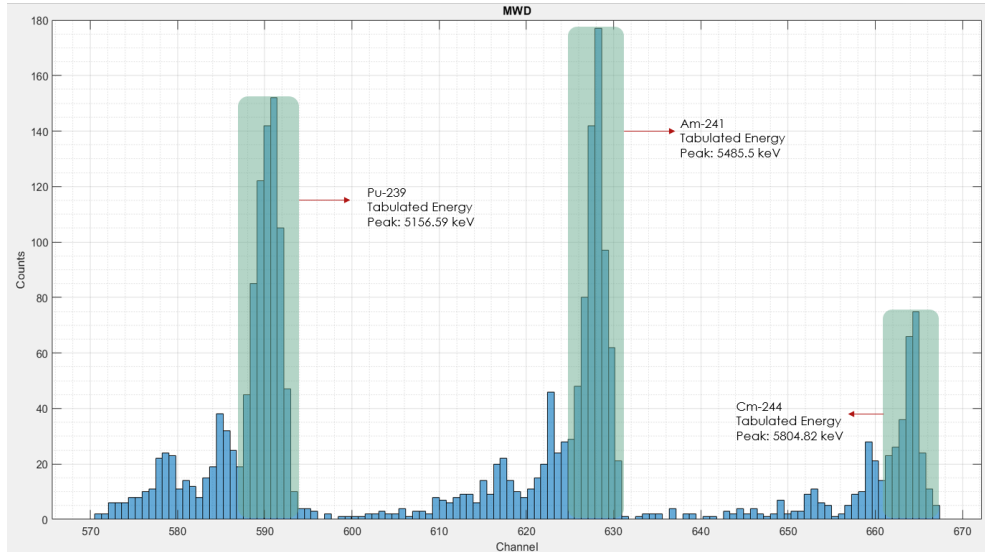


Figure 37. Histogram consisting of 100 bars. The main peaks of radionuclides are shown in turquoise colour. Energy values of the main peaks are shown.

When the data in the Counts / Channel histogram chart was analysed using the OriginLab program, the values in Table 4 were obtained. While calculating the uncertainty for the total count in the net area, it was made by the square root of the count (Equation 42) [33]. While calculating the error of the FWHM value, the channel amount corresponding to a histogram bar is calculated. This value is approximately 0.97. Using Equation 43, the FWHM error was calculated as  $\pm 0.69$ .

$$\text{Area Error (Count)} = \sqrt{\text{Area (count)}} \quad \text{Equation 42}$$

$$\text{FWHM Error (ch)} = \sqrt{\left(\frac{0.97}{2}\right)^2 + \left(\frac{0.97}{2}\right)^2} \quad \text{Equation 43}$$

Table 4. Results of Moving Window Deconvolution filter obtained using OriginLab program. It shows the net area, FWHM, peak height and peak centre.

	<b>Area (count)</b>	<b>Area Error (count)</b>	<b>FWHM (ch)</b>	<b>FWHM Error (ch)</b>	<b>Centre (ch)</b>	<b>Height (count)</b>
<b>1</b>	811.89	28.49	3.97	0.69	590.00	196.00
<b>2</b>	771.15	27.77	2.97	0.69	627.83	214.00
<b>3</b>	325.44	18.04	2.71	0.69	663.72	93.00

A calibration was performed to convert the histogram created with Count/Channel data into a histogram displayed with Count/Energy data. Main energy peaks of Pu-239 and Am-241 radionuclides shown in Table 5 were Pu-239 at

an energy of 5156.59 keV and channel values of 591, and 628.3 corresponding to Am-241 radionuclide at an energy level of 5485.5 keV [9].

*Table 5. The calibration values used to switch from the Counts / Channel histogram to the Counts / Energy histogram.*

Centroid Channel of the Peak	591	628.3
Energy (keV)	5156.59	5485.5
Radionuclide Name	Pu-239	Am-241
Fraction of the Main Peak (%)	73.3	84.5

Equation 44 is obtained according to the graph shown in the Figure 38. After applying the calibration equation to all channel values, the Count/Energy histogram shown in Figure 39 was obtained.

$$y = 8.818x - 54.826$$

Equation 44

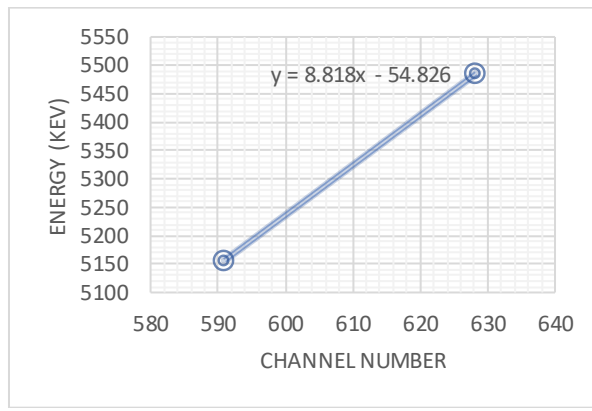


*Figure 38. Linear line equation and linear line created by the main peaks used for calibration*

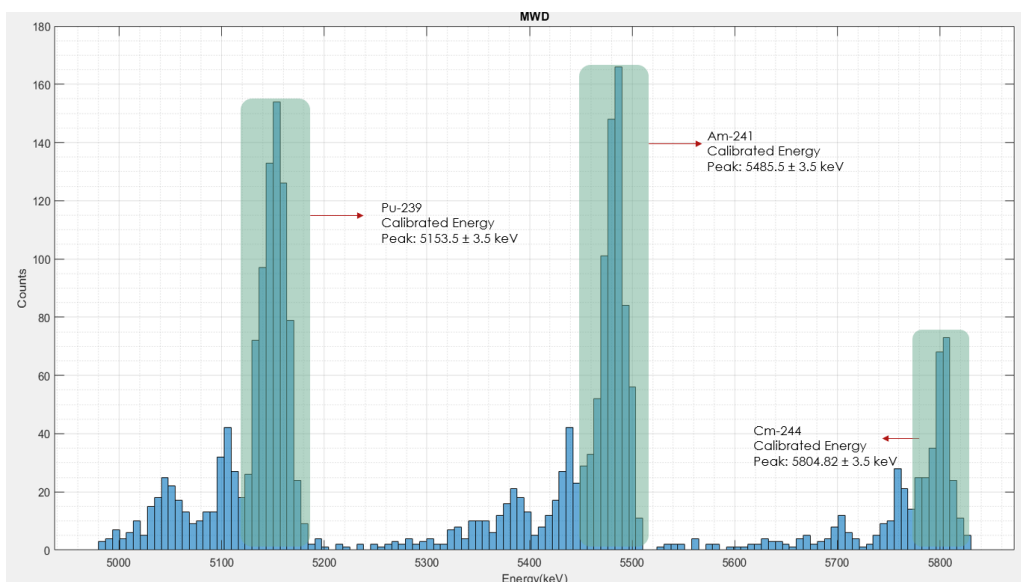


*Figure 39. Histogram shown with energy data. The energy values of radionuclides are specified. These energy values are calculated values. The parts shown in turquoise colour are the main peaks of radionuclides*

## 7. Trapezoidal Filter Parameter Optimization

Using the step function signal obtained in Section 4 of Chapter 3 is applied according to the Equation 41 (trapezoidal filter equation) related to the trapezoidal filter mentioned in Section 4 of Chapter 3. There are two different parameters at this stage. Of these, it is used for the flat top part named with the letter M and the length L is both the rising time and the moving average length. First of all, one of the trapezoidal shapes obtained by applying different values of flat top length is shown in Figure 40 using purple colour.

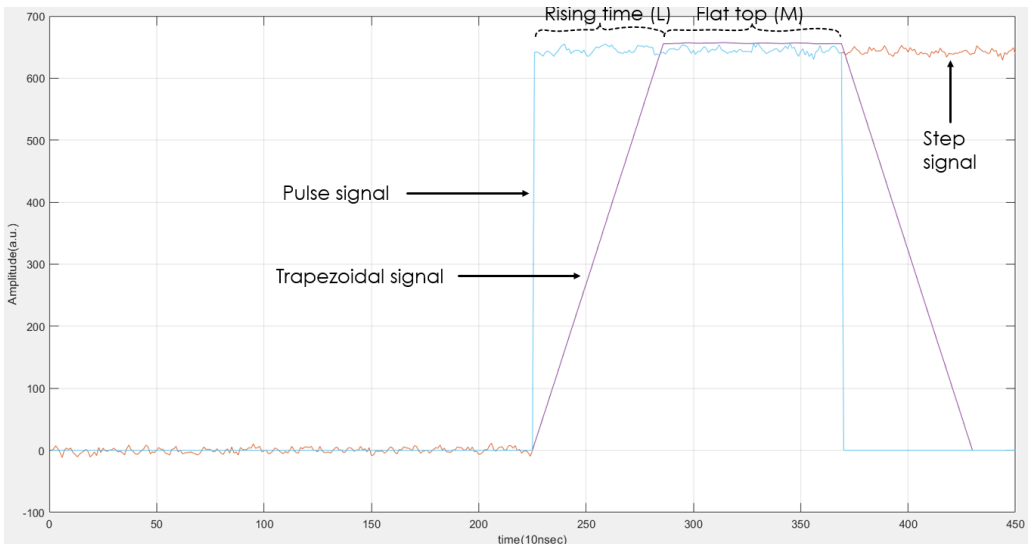


*Figure 40. The trace shown in orange is a step signal obtained by applying deconvolution of the signal from the ADC. The trace shown in blue is a pulse signal. For the trapezoidal filter, the signal has a width up to the desired point of use. The remaining data are discarded. The trace shown in purple is the trapezoidal filtered signal*

The next step was to find out how the flat top time parameter affects the FWHM values of the energy peaks in the histogram, the trend behaviour and determine the optimum value. For this, the rising time parameter was determined at a fixed time of 0.05 microseconds. 5 was used for the "w" variable used in the codes shown in Appendix 8 and 9. In other words, this means that the average of 5 data (50 nanoseconds) is taken to continue. In other words, "w" is the window length used for averaging [32]. Table 6, Table 7 and Table 8 contain information on the main peaks obtained from the histogram of Pu-239, Am-241 and Cm-244 radionuclides, respectively.

*Table 6. The data of Pu-239 peak are shown using the OriginLab Pro program. The flat top time value is varied while keeping the Rise time at a constant value. The FWHM, total peak area count, centre of the peak and height of the peak data are presented*

	m	w	Rise Time(μsec)	Flat Time(μsec)	Area (count)	Area Error (count)	FWHM (ch)	Center (ch)	Height (count)
1	20.00	5.00	0.05	2.00	841.00	29.00	3.82	709.20	214.00
2	70.00	5.00	0.05	1.50	840.42	28.99	4.29	709.20	194.00
3	95.00	5.00	0.05	1.25	862.46	29.37	4.30	709.20	194.00
4	145.00	5.00	0.05	0.75	857.82	29.29	4.21	709.20	179.00
5	170.00	5.00	0.05	0.50	842.74	29.03	4.38	709.20	183.00
6	195.00	5.00	0.05	0.25	924.52	30.41	5.05	709.20	169.00
7	215.00	5.00	0.05	0.05	969.18	31.13	6.81	711.52	115.00

*Table 7. The data of Am-241 peak are shown using the OriginLab Pro program. The flat top time value is varied while keeping the Rise time at a constant value. The FWHM, total peak area count, centre of the peak and height of the peak data are presented.*

	m	w	Rise Time(μsec)	Flat Time(μsec)	Area (count)	Area Error (count)	FWHM (ch)	Center (ch)	Height (count)
1	20.00	5.00	0.05	2.00	776.62	27.87	2.95	754.44	224.00
2	70.00	5.00	0.05	1.50	783.58	27.99	2.99	754.44	224.00
3	95.00	5.00	0.05	1.25	749.94	27.39	3.87	754.44	186.00
4	145.00	5.00	0.05	0.75	919.88	30.33	4.04	754.44	180.00
5	170.00	5.00	0.05	0.50	806.20	28.39	4.08	753.28	182.00
6	195.00	5.00	0.05	0.25	943.66	30.72	4.70	753.28	160.00
7	215.00	5.00	0.05	0.05	890.30	29.84	8.28	750.96	109.00

*Table 8. The data of Cm-244 peak are shown using the OriginLab Pro program. The flat top time value is varied while keeping the Rise time at a constant value. The FWHM, total peak area count, centre of the peak and height of the peak data are presented.*

	m	w	Rise Time(μsec)	Flat Time(μsec)	Area (count)	Area Error (count)	FWHM (ch)	Center (ch)	Height (count)
1	20.00	5.00	0.05	2.00	303.34	17.42	2.85	797.36	93.00
2	70.00	5.00	0.05	1.50	304.50	17.45	3.06	797.36	88.00
3	95.00	5.00	0.05	1.25	287.68	16.96	3.78	798.52	76.00
4	145.00	5.00	0.05	0.75	284.20	16.86	3.70	798.52	78.00
5	170.00	5.00	0.05	0.50	301.60	17.37	3.97	797.36	75.00
6	195.00	5.00	0.05	0.25	305.08	17.47	4.05	797.36	75.00
7	215.00	5.00	0.05	0.05	306.82	17.52	5.17	793.88	55.00

When the results obtained from the main peaks of three different radionuclides were examined, the line graph shown in Figure 41 was obtained according to the FWHM data. When the trends are analysed, it is seen that the length of the flat top increases and the FWHM values tend to decrease. As a result, the longest possible flat top time is best to achieve the least FWHM. Therefore, 2 microseconds long flat top was determined. Equation 42 and 43 were used to calculate the uncertainties [33]. So for FWHM in histograms the error is  $\pm 0.69$ .

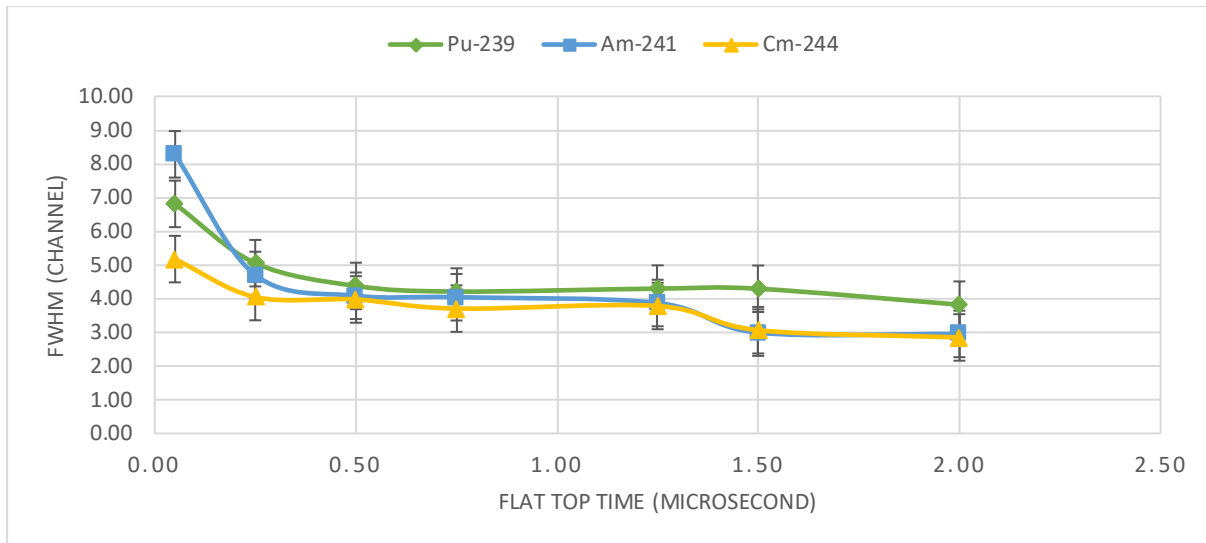


Figure 41. Line graph obtained according to the changing flat top time values of FWHM (channel) data. It is shown for three different radionuclides. The line in green represents Pu-239, the line in blue represents Am-241, and the line in yellow represents the Cm-244 radionuclide.

In the next step of the study, it is aimed to find the behaviour and optimum value of the rise time parameter. First of all, the rise time parameter has been changed so that the optimum result for flat top time is fixed. The properties of the main peaks of three different radionuclides obtained from the histogram are shown in Table 9, Table 10 and Table 11, Pu-239, Am-241 and Cm-244, respectively.

Table 9. The data of Pu-239 peak are shown using the OriginLab Pro program. The rise time value is varied while keeping the flat top time at a constant value. The FWHM, total peak area count, centre of the peak and height of the peak data are presented.

	m	w	Rise Time(μsec)	Flat Time(μsec)	Area (count)	Area Error (count)	FWHM (ch)	Center (ch)	Height (count)
1	23.00	2.00	0.02	2	816.06	28.57	4.50542	709.2	193
2	21.00	4.00	0.04	2	815.48	28.56	4.32406	709.2	192
3	19.00	6.00	0.06	2	838.68	28.96	4.07262	709.2	207
4	17.00	8.00	0.08	2	841.58	29.01	4.15259	709.2	214
6	13.00	12.00	0.12	2	809.68	28.45	4.1732	709.2	205
7	11.00	14.00	0.14	2	818.38	28.61	4.07967	709.2	195
8	9.00	16.00	0.16	2	812	28.50	3.87968	709.2	202

*Table 10. The data of Am-241 peak are shown using the OriginLab Pro program. The rise time value is varied while keeping the flat top time at a constant value. The FWHM, total peak area count, centre of the peak and height of the peak data are presented.*

	m	w	Rise Time(μsec)	Flat Time(μsec)	Area (count)	Area Error (count)	FWHM (ch)	Center (ch)	Height (count)
1	23.00	2.00	0.02	2	789.96	28.11	3.45397	754.44	206
2	21.00	4.00	0.04	2	790.54	28.12	3.43523	754.44	208
3	19.00	6.00	0.06	2	807.94	28.42	3.48481	754.44	204
4	17.00	8.00	0.08	2	773.72	27.82	3.19729	754.44	217
6	13.00	12.00	0.12	2	779.52	27.92	2.84472	754.44	232
7	11.00	14.00	0.14	2	785.9	28.03	2.82368	754.44	233
8	9.00	16.00	0.16	2	783	27.98	2.809	754.44	234

*Table 11. The data of Cm-244 peak are shown using the OriginLab Pro program. The rise time value is varied while keeping the flat top time at a constant value. The FWHM, total peak area count, centre of the peak and height of the peak data are presented.*

	m	w	Rise Time(μsec)	Flat Time(μsec)	Area (count)	Area Error (count)	FWHM (ch)	Center (ch)	Height (count)
1	23.00	2.00	0.02	2	307.98	17.55	3.43193	797.36	78
2	21.00	4.00	0.04	2	309.14	17.58	3.25758	798.52	81
3	19.00	6.00	0.06	2	289.42	17.01	3.24214	797.36	102
4	17.00	8.00	0.08	2	313.2	17.70	2.76467	797.36	91
6	13.00	12.00	0.12	2	290	17.03	2.52714	797.36	98
7	11.00	14.00	0.14	2	304.5	17.45	2.51269	797.36	94
8	9.00	16.00	0.16	2	304.5	17.45	2.45181	797.36	95

The line chart of rise time parameters changing according to the FWHM values is shown in Figure 42. The lowest FWHM value is at 0.16 microseconds rise time. Equation 42 and 43 were used to calculate the uncertainties. So for FWHM in histograms the error is  $\pm 0.69$ .

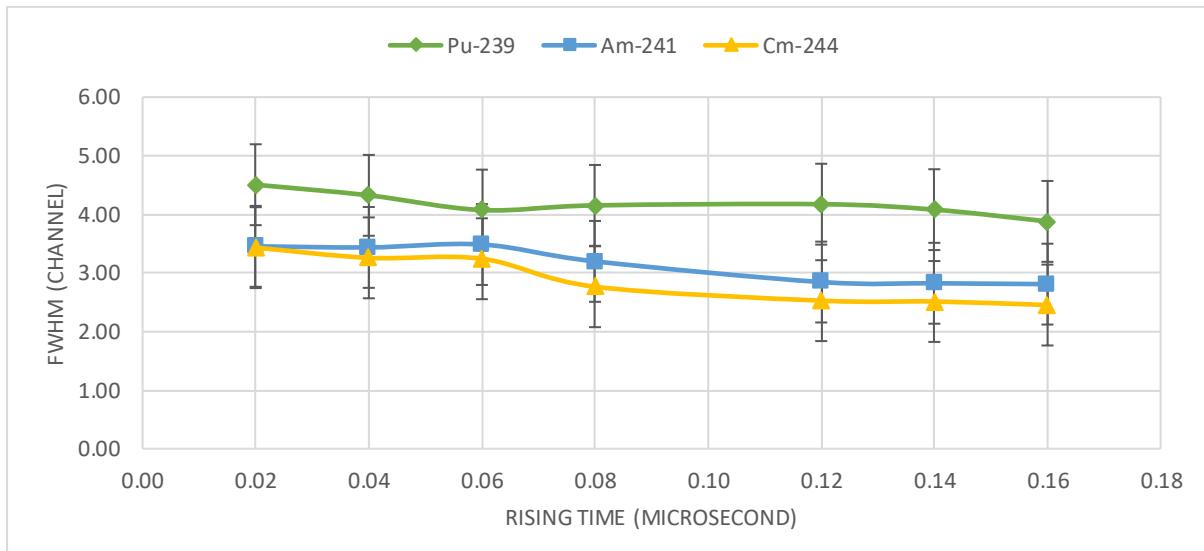


*Figure 42. Line chart obtained according to changing rising time values of FWHM (channel) data. It is shown for three different radionuclides. The green line represents Pu-239, the blue line represents Am-241 and the yellow colour represents the Cm-244 radionuclide*

## 8. Histogram Creation

The Counts / Channel graph shown in Figure 43 was created using optimum flat top time and rising time values. The calibration for Figure 44 was based on Pu-239 and Am-241. As seen in Table 12, the main peak central channel values of both nuclides are 627.6 and 667.8 channels, respectively.

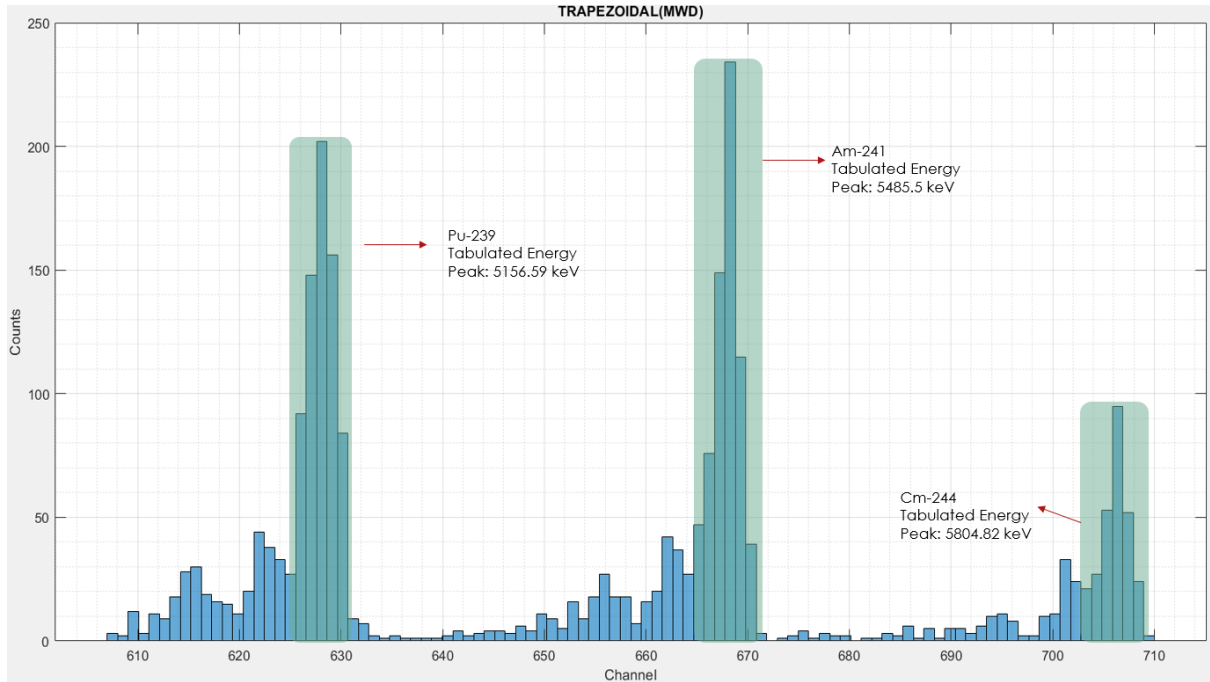


Figure 43. Histogram created with a trapezoidal filter using the optimum flat top time and rising time parameters. It consists of 100 bars.

Table 12. Table of values used to transform from histogram with channel data to histogram with energy data.

Centroid Channel of the Peak	627.6	667.8
Energy (keV)	5156.59	5485.5
Radionuclide Name	Pu-239	Am-241
Fraction of the Main Peak (%)	73.3	84.5

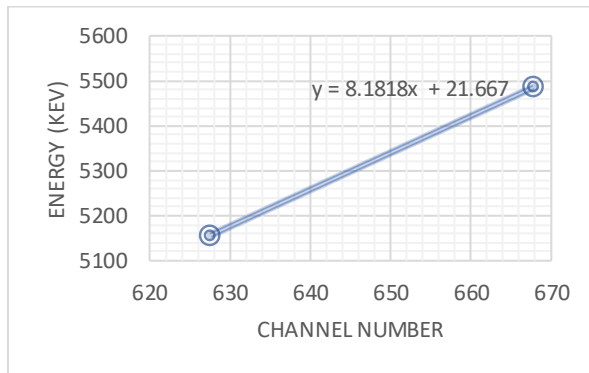


Figure 44. Linear equation and linear line created according to the channel data of the peak of two main peaks

The equation obtained because of the calibration calculation is Equation 45. The Counts / Energy histogram obtained using the algorithm can be examined in Appendix 9 is shown in Figure 45.

$$y = 8.1818x + 21667$$

Equation 45

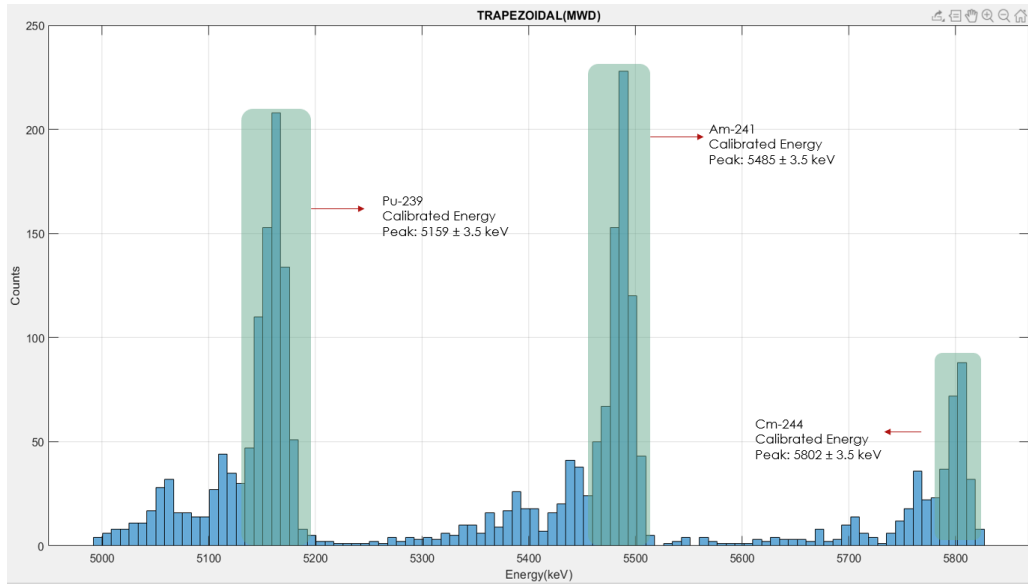


Figure 45. Histogram obtained with a trapezoidal filter and shown with energy data. The energy values of radionuclides are specified. These energy values are calculated values. The parts shown in turquoise colour are the main peaks of radionuclides.

## 9. Discussion

The energy histogram of the alpha radiations emitted from the radionuclides Pu-239, Am-241 and Cm-244 was created. The parameters of the filters used were optimized in order to keep the FWHM value at the minimum level among the obtained results. When the findings were examined, it was seen that the trapezoidal filter technique offered a better resolution than the moving window deconvolution technique. In the examinations made, the smoother the upper side of the signal shows that the trapezoidal filter gives better results. The FWHM results of the moving window deconvolution filter were  $3.97 \pm 0.69$  channels,  $2.97 \pm 0.69$  channels, and  $2.71 \pm 0.69$  channels, for Pu-239, Am-241 and Cm-244, respectively. The optimum FWHM result found with the trapezoidal filter was  $3.87 \pm 0.69$  for Pu-239,  $2.80 \pm 0.69$  for Am-241 and  $2.45 \pm 0.69$  for Cm-244.

When the time constant optimizations obtained are examined, the optimum result for the exponential rising part is 6.59 microseconds. The optimum result obtained for the exponential decay piece is 38.86 microseconds.

The greater the number of counts, the less uncertainty would have been obtained. When the optimum results of the FWHM values are examined, the amount of 0.69 channel uncertainty can be reduced by creating more histogram bins. However, as more histograms are created, gaps occur at the peaks. The optimum histogram peak width is determined as approximately 7-8 keV. These histogram bins are adequate, allowing the peaks to be seen by eye. If more counts had been obtained, the histogram bin width could have been reduced and as a result, the uncertainty value decreased.

In double-sided silicon strip detectors, some alpha particles enter the spaces between the strips. Since no excess load is collected, energy loss occurs, less load is perceived. Therefore, lower-energy artefact peaks are seen before the main peaks of radionuclides. These peaks are not included in the alpha radiation energies of Pu-239, Am-241 and Cm-244. However, this situation did not affect the analysis. The spectrum (Figure 46) obtained in a previous study is shown. In this study, peaks are not observed at low energies caused by a double-sided silicon detector.

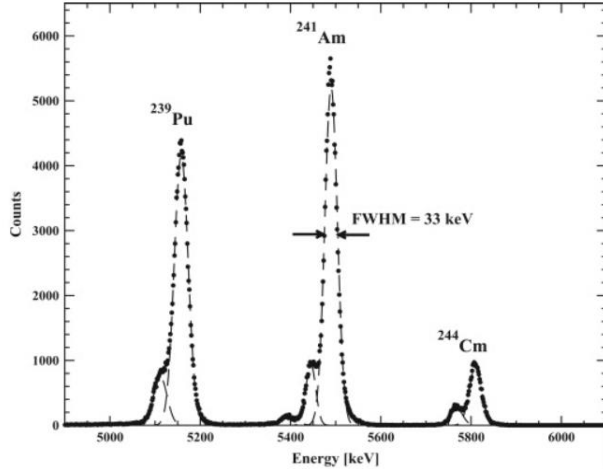


*Figure 46. A spectrum consisting of Pu-239, Am-241 and Cm-244 main peaks (Provided from ref. [34].)*

When the trapezoidal filter results are examined, it gives the best resolution with the highest possible flat top time. Likewise, the higher the time, the better the resolution. In other words, getting more data and more averages led to a lower FWHM value. The optimum results were determined as 2 microseconds for flat top time and 0.16 microsecond for rising time. When the results are examined in general, fluctuation is seen among some values. However, reasonable results were obtained when uncertainty values were included.

Main peaks were obtained as an average of 200 counts, while fine-structure peaks had approximately 30-40 counts. The decomposition of these peaks is very important. Even the separation of alpha peaks with lower fraction shows that the resolution is high. The Am-241 and Cm-244 peaks look pretty good, but the Pu-239 peak looks wider than it should be because there is not a single peak but two lines of alpha decay close to each other. These do not have the same intensity, so the FWHM value seems to be higher.

## CHAPTER 5: CONCLUSION

It is aimed to obtain minimum FWHM values by using moving window deconvolution and trapezoidal filter for histograms created at alpha-particle energies detected in the double-sided silicon strip detector used in the project. For this purpose, the most optimum parameters of digital signal processing filters used were investigated. Since only one strip of the double-sided silicon strip detector is used, it has similar characteristics to the silicon detector.

Digital signal processing steps are shown in Figure 47. Among the filters used, moving window deconvolution gave higher FWHM values than trapezoidal filters. For optimization of time constants, 6.59 microsecond for exponential rising part and 38.86 microsecond for exponential decay part were found. The optimum trapezoidal filter parameters were found to be 2 microseconds for flat top time and 0.16 microsecond for rising time.

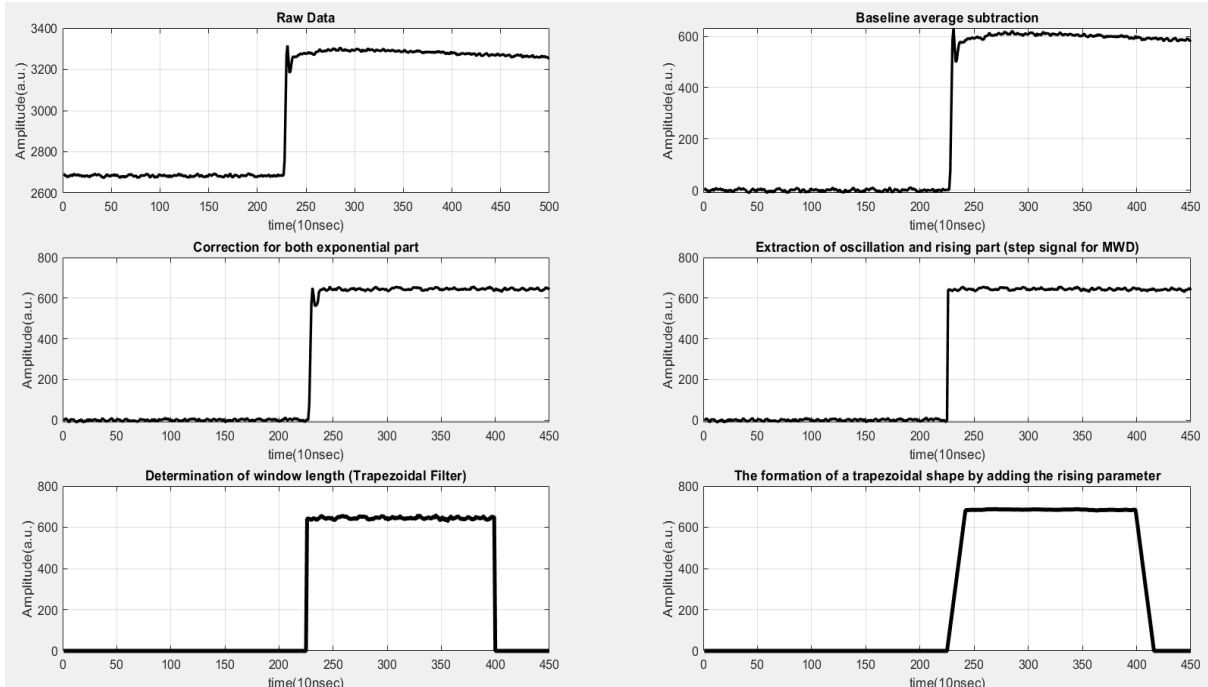


*Figure 47. The change of the signal is shown for the moving window deconvolution filter and the trapezoidal filter. a) The trace shown at the top left is the digitized signal given by the Analogue Digital Converter and has not been added to any software yet. b) The trace shown at the top right is the signal obtained by subtracting the baseline level from the raw trace. The proportional amplitude value of the alpha energy is clearly seen as it is extracted from the baseline. c) It is the signal that is corrected after the optimum time constants for both exponential rising part and exponential decay part are determined. d) It is the step signal, which is the last step in the MWD filter. Unused parts have been discarded from the signal. The average of the high part of the signal directly gives the proportional amplitude value of the alpha particle. The histogram is the signal used to create. e) For the trapezoidal filter, the signal is clipped, and a pulse signal is formed. It determines the flat top time. e) It is the signal that occurs when the edges of the pulse signal become trapezoid after averaging in the window width determined for the formation of a trapezoidal filter. It is the last signal of the trapezoidal filter before the histogram is created.*

As a result, radiation must interact with matter to perceive it. Thanks to the silicon semiconductor used, the energy of the alpha particle entered the

spectroscopy system. The signal generated as a result of the change in the chemical structure has been processed using nuclear electronic components. Primarily, the analogue signal is amplified using a pre-amplifier. Afterwards, it was digitized thanks to the analogue-digital converter, and the ability to operate in digital environment was gained. Using the MATLAB application, histograms were created using moving window deconvolution and trapezoidal filters, resulting in visuality for alpha spectroscopy. Meanwhile, optimum parameters giving the lowest FWHM value for the best resolution were determined.

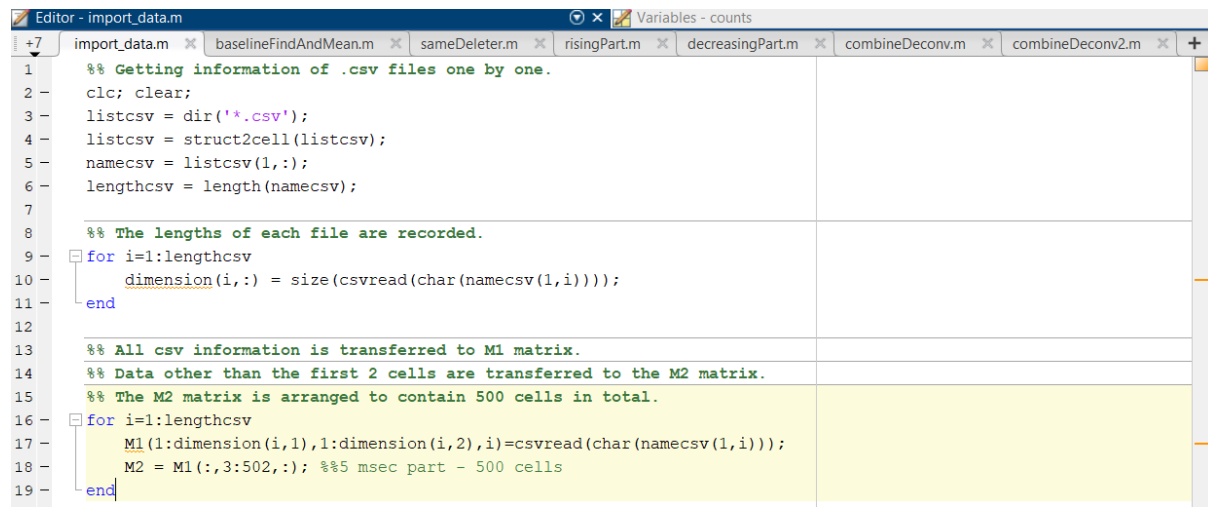
## FUTURE WORK

Since no more data could be collected due to Covid-19, the silicon detector could not be used. In future studies, data can be collected using a simpler silicon detector. Thus, more original spectrum can be obtained. In addition, higher precision can be obtained by making more measurements.

The studies can be simultaneously run in a computer environment and the results can be displayed on the screen. In this way, faster results and faster analysis can be done. It can also speed up the system and generate a characterized preamplifier response function.

## APPENDIXES

### APPENDIX 1: Transferring and storing all data files to MATLAB environment



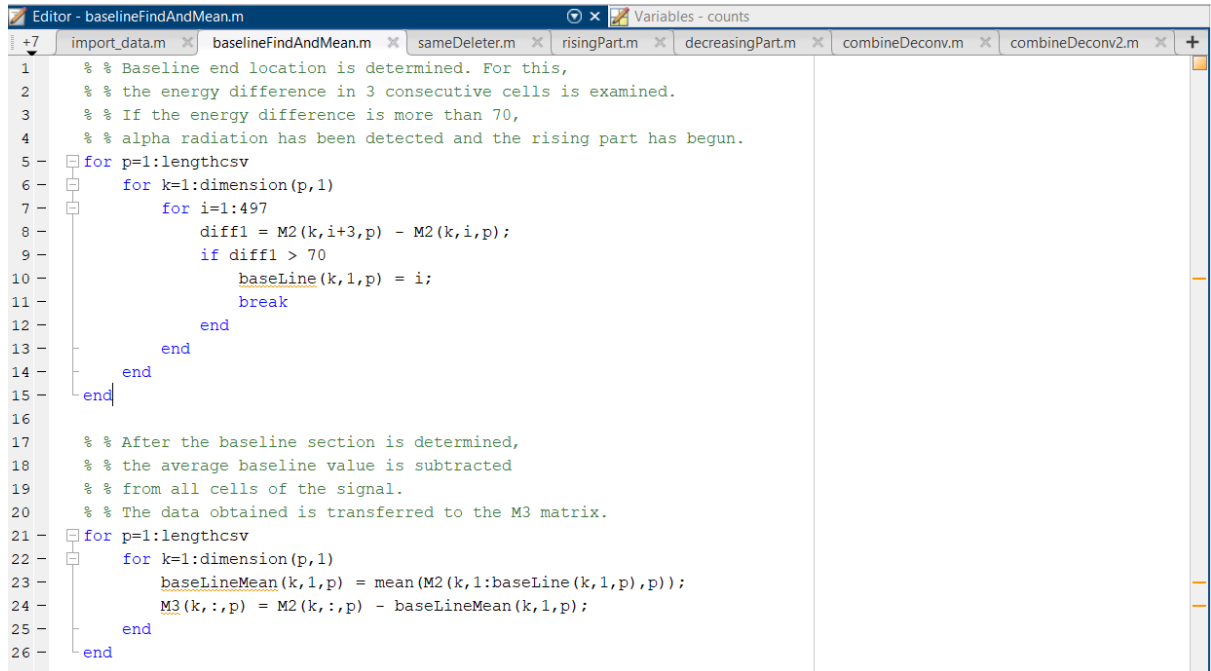
The screenshot shows the MATLAB Editor window with the file `import_data.m` open. The code is used to transfer and store data from CSV files into MATLAB matrices `M1` and `M2`. The code uses `for` loops to iterate through the CSV files and `csvread` to read the data. It also uses `size` and `struct2cell` functions to handle the file names and dimensions.

```
% Getting information of .csv files one by one.
clc; clear;
listcsv = dir('*.*');
listcsv = struct2cell(listcsv);
namecsv = listcsv(1,:);
lengthcsv = length(namecsv);

% The lengths of each file are recorded.
for i=1:lengthcsv
    dimension(i,:) = size(csvread(char(namecsv(1,i))));
end

% All csv information is transferred to M1 matrix.
% Data other than the first 2 cells are transferred to the M2 matrix.
% The M2 matrix is arranged to contain 500 cells in total.
for i=1:lengthcsv
    M1(1:dimension(i,1),1:dimension(i,2),i)=csvread(char(namecsv(1,i)));
    M2 = M1(:,3:502,:); %%5 msec part - 500 cells
end
```

## APPENDIX 2: Determining the end point of the baseline and taking its average and recording



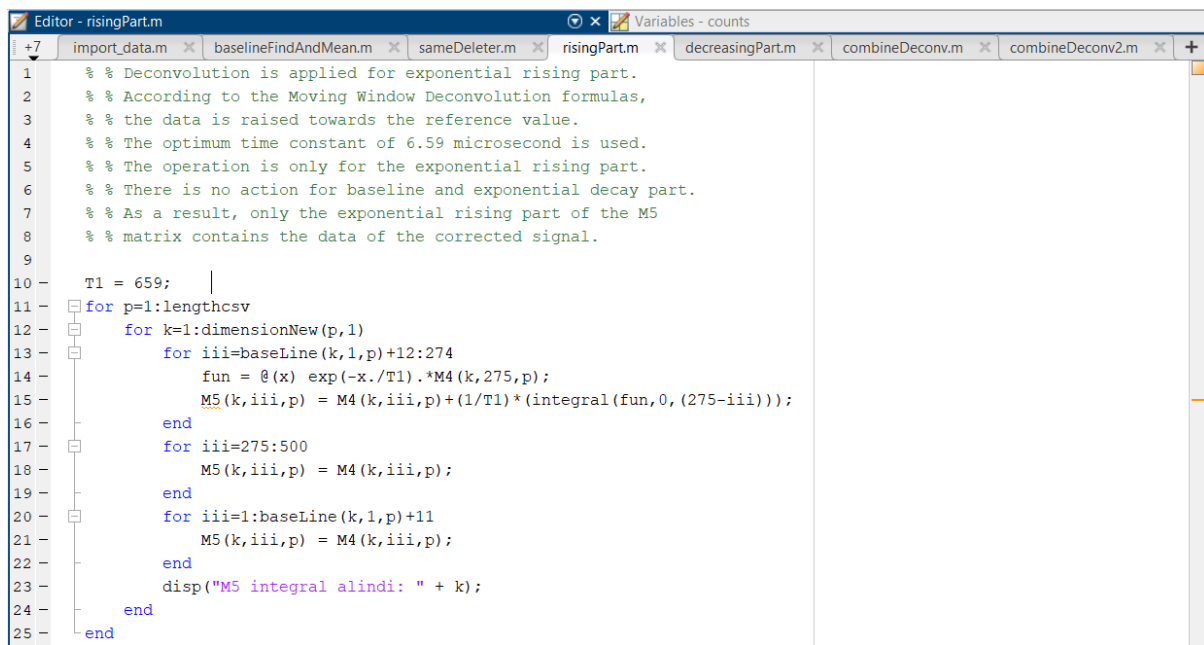
```

Editor - baselineFindAndMean.m
Variables - counts
import_data.m baselineFindAndMean.m sameDeleter.m risingPart.m decreasingPart.m combineDeconv.m combineDeconv2.m + 

1 % % Baseline end location is determined. For this,
2 % % the energy difference in 3 consecutive cells is examined.
3 % % If the energy difference is more than 70,
4 % % alpha radiation has been detected and the rising part has begun.
5 for p=1:lengthcsv
6     for k=1:dimension(p,1)
7         for i=1:497
8             diff1 = M2(k,i+3,p) - M2(k,i,p);
9             if diff1 > 70
10                 baseLine(k,1,p) = i;
11                 break
12             end
13         end
14     end
15 end
16
17 % % After the baseline section is determined,
18 % % the average baseline value is subtracted
19 % % from all cells of the signal.
20 % % The data obtained is transferred to the M3 matrix.
21 for p=1:lengthcsv
22     for k=1:dimension(p,1)
23         baseLineMean(k,1,p) = mean(M2(k,1:baseLine(k,1,p),p));
24         M3(k,:,:p) = M2(k,:,:p) - baseLineMean(k,1,p);
25     end
26 end

```

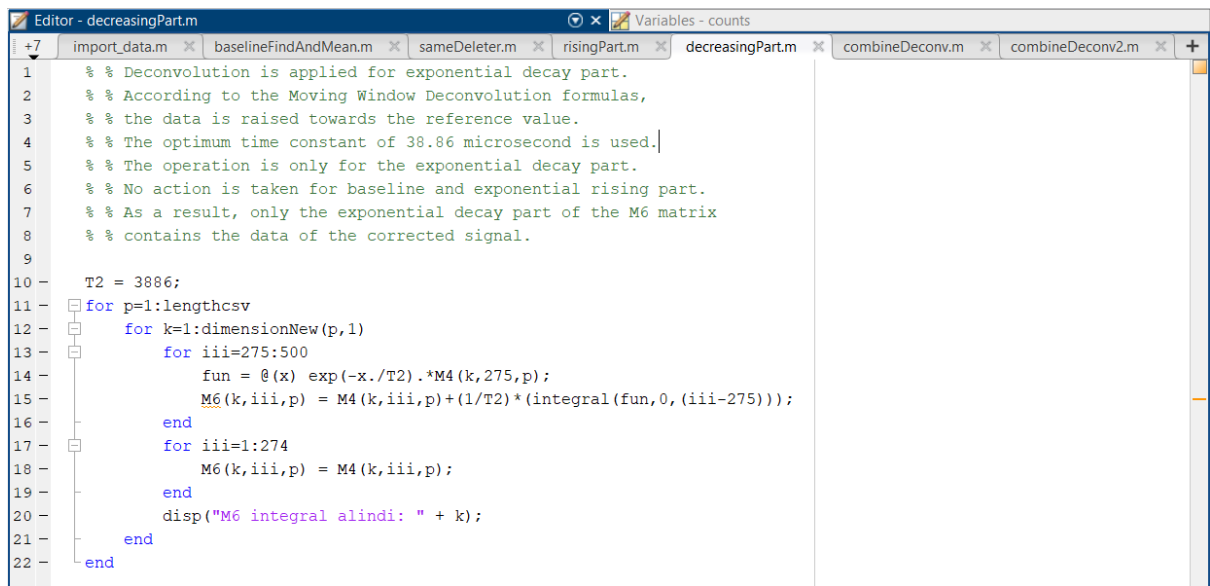
### APPENDIX 3: Correction for exponential rising part



The screenshot shows the MATLAB Editor window titled "Editor - risingPart.m". The tab bar at the top includes "Variables - counts" and several other files: "import\_data.m", "baselineFindAndMean.m", "sameDeleter.m", "risingPart.m" (which is the active file), "decreasingPart.m", "combineDeconv.m", and "combineDeconv2.m". The code in the editor is as follows:

```
1 % % Deconvolution is applied for exponential rising part.
2 % % According to the Moving Window Deconvolution formulas,
3 % % the data is raised towards the reference value.
4 % % The optimum time constant of 6.59 microsecond is used.
5 % % The operation is only for the exponential rising part.
6 % % There is no action for baseline and exponential decay part.
7 % % As a result, only the exponential rising part of the M5
8 % % matrix contains the data of the corrected signal.
9
10 T1 = 659; |
11 for p=1:lengthcsv
12     for k=1:dimensionNew(p,1)
13         for iii=baseLine(k,1,p)+12:274
14             fun = @(x) exp(-x./T1).*M4(k,275,p);
15             M5(k,iii,p) = M4(k,iii,p)+(1/T1)*(integral(fun,0,(275-iii)));
16         end
17         for iii=275:500
18             M5(k,iii,p) = M4(k,iii,p);
19         end
20         for iii=1:baseLine(k,1,p)+11
21             M5(k,iii,p) = M4(k,iii,p);
22         end
23         disp("M5 integral alindi: " + k);
24     end
25 end
```

## APPENDIX 4: Correction for exponential decay part



The screenshot shows the MATLAB Editor window with the file 'decreasingPart.m' open. The code performs deconvolution on an exponential decay part of a signal. It uses nested loops to iterate over dimensions and calculate integrals. A warning message is displayed in the command window.

```
% % Deconvolution is applied for exponential decay part.
% % According to the Moving Window Deconvolution formulas,
% % the data is raised towards the reference value.
% % The optimum time constant of 38.86 microsecond is used.
% % The operation is only for the exponential decay part.
% % No action is taken for baseline and exponential rising part.
% % As a result, only the exponential decay part of the M6 matrix
% % contains the data of the corrected signal.

T2 = 3886;
for p=1:lengthcsv
    for k=1:dimensionNew(p,1)
        for iii=275:500
            fun = @(x) exp(-x./T2).*M4(k,275,p);
            M6(k,iii,p) = M4(k,iii,p)+(1/T2)*(integral(fun,0,(iii-275)));
        end
        for iii=1:274
            M6(k,iii,p) = M4(k,iii,p);
        end
        disp("M6 integral alindi: " + k);
    end
end
```

## APPENDIX 5: Merging of exponential rising part and exponential decay part

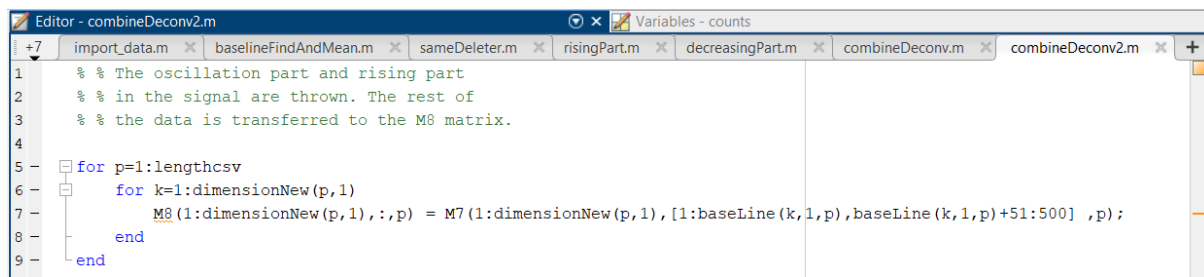
The screenshot shows the MATLAB Editor window with the file 'combineDeconv.m' open. The code is a script for merging two parts of a deconvolution process. It includes comments explaining the purpose of each section and uses nested loops to iterate through data points and parameters.

```

Editor - combineDeconv.m*
import_data.m baselineFindAndMean.m sameDeleter.m risingPart.m decreasingPart.m combineDeconv.m* combineDeconv2.m + Variables - counts
+7 import_data.m baselineFindAndMean.m sameDeleter.m risingPart.m decreasingPart.m combineDeconv.m* combineDeconv2.m +
1 % % In this part of the algorithm, both the exponential
2 % % rising part and the exponential decay part are processed
3 % % simultaneously. The resulting correction work is transferred
4 % % to the M7 integral. So the data where the two parts are combined is M7.
5 %% DECAY CONSTANT ---- FIRST PART COMBINE
6 T1 = 659;
7 for p=1:lengthcsv
8     for k=1:dimensionNew(p,1)
9         for iiii=baseLine(k,1,p)+12:274
10            fun = @(x) exp(-x./T1).*M4(k,275,p);
11            M7(k,iiii,p) = M4(k,iiii,p)+(1/T1)*(integral(fun,0,(275-iiii)));
12        end
13        for iiii=1:baseLine(k,1,p)+11
14            M7(k,iiii,p) = M4(k,iiii,p);
15        end
16        disp("M7+ integral alindi: " + k);
17    end
18 end
19 %% DECAY CONSTANT ---- SECOND PART COMBINE
20 T2 = 3886;
21 for p=1:lengthcsv
22     for k=1:dimensionNew(p,1)
23         for iiii=275:500
24             fun = @(x) exp(-x./T2).*M4(k,275,p);
25             M7(k,iiii,p) = M4(k,iiii,p)+(1/T2)*(integral(fun,0,(iiii-275)));
26         end
27         disp("M7- integral alindi: " + k);
28     end
29 end

```

## APPENDIX 6: Removing the oscillation part and rising part from traces



The screenshot shows the MATLAB Editor window with the file 'combineDeconv2.m' open. The code is as follows:

```
% % The oscillation part and rising part
% % in the signal are thrown. The rest of
% % the data is transferred to the M8 matrix.
for p=1:lengthcsv
    for k=1:dimensionNew(p,1)
        M8(1:dimensionNew(p,1),:,p) = M7(1:dimensionNew(p,1),[1:baseLine(k,1,p),baseLine(k,1,p)+51:500] ,p);
    end
end
```

## APPENDIX 7: Generating histograms from the results of the MWD algorithm

The image shows two screenshots of the MATLAB Editor window. Both screenshots have tabs at the top: sameDeleter.m, risingPart.m, decreasingPart.m, combineDeconv.m, combineDeconv2.m, histogramMWD.m\*, and a plus sign icon.

**Screenshot 1 (Top):**

```

1 % % In this software part, the first three data are extracted,
2 % % the baseline average is extracted from all data and the trace
3 % % is of the type of step signal. First of all, in this algorithm,
4 % % M9 matrix contains the maximum data of MWD. That is, the higher
5 % % parts of the signals are averaged and recorded. Then all the
6 % % traces obtained are taken from all files and stored in the
7 % % MhistogramMwd matrix. This matrix is where all the data comes
8 % % together to create a histogram. The histogram of Counts / Channel
9 % % type is created with MhistogramMwd. Then, using the slope and
10 % % intercept of the linear equation produced for calibration,
11 % % the MEnergyMwd matrix is created. This matrix is the matrix where
12 % % histogram information of type Counts / Energy is stored.
13 % combineDeconv2;
14 for p=1:lengthcsv
15     for k=1:dimensionNew(p,1)
16         M9(k,1,p) = mean(M8(k,baseLine(k,1,p)+51:end,p));
17     end
18 end
19 MhistogramMwd = [M9(1:dimensionNew(1,1),1,1);
20     M9(1:dimensionNew(2,1),1,2);
21     M9(1:dimensionNew(3,1),1,3);
22     M9(1:dimensionNew(4,1),1,4);
23     M9(1:dimensionNew(5,1),1,5);
24     M9(1:dimensionNew(6,1),1,6);
25     M9(1:dimensionNew(7,1),1,7);
26     M9(1:dimensionNew(8,1),1,8);
27     M9(1:dimensionNew(9,1),1,9);
28     M9(1:dimensionNew(10,1),1,10);
29     M9(1:dimensionNew(11,1),1,11)];
30

```

**Screenshot 2 (Bottom):**

```

19 MhistogramMwd = [M9(1:dimensionNew(1,1),1,1);
20     M9(1:dimensionNew(2,1),1,2);
21     M9(1:dimensionNew(3,1),1,3);
22     M9(1:dimensionNew(4,1),1,4);
23     M9(1:dimensionNew(5,1),1,5);
24     M9(1:dimensionNew(6,1),1,6);
25     M9(1:dimensionNew(7,1),1,7);
26     M9(1:dimensionNew(8,1),1,8);
27     M9(1:dimensionNew(9,1),1,9);
28     M9(1:dimensionNew(10,1),1,10);
29     M9(1:dimensionNew(11,1),1,11)];
30
31 figure(150); histogram(MhistogramMwd(:,1),125);
32 title('MWD'); xlabel('Channel'); ylabel('Counts');
33 hold on; grid on; grid minor;
34 MEnergyMwd(:,1) = 8.818*MhistogramMwd(:,1)-54.826;
35 figure(160); histogram(MEnergyMwd(:,1),125);
36 title('MWD'); xlabel('Energy(keV)'); ylabel('Counts');
37 hold on; grid on; grid minor; ax.MinorGridLineStyle = '-';
38

```

## APPENDIX 8: Determining the parameters of the trapezoidal filter and determining the proportional difference in amplitude

```

Editor - trapezoid.m
Variables - counts
+ sameDeleter.m | risingPart.m | decreasingPart.m | combineDeconv.m | combineDeconv2.m | histogramMWD.m | trapezoid.m | + | 

1 % % The variable m produced for the algorithm
2 % % is a factor in determining the flat top time.
3 % % The w parameter is another variable produced
4 % % for the algorithm and represents the window
5 % % width used for averaging. The length of
6 % % m is subtracted from the applicable data set.
7 % % The remaining amount of data is processed.
8 % % This part of the algorithm is operated only
9 % % when a Trapezoidal filter is required. Therefore,
10 % % M10 matrix is the matrix containing trapezoidal shape.
11
12 - m = 9;      % width of step pulse
13 - w = 16;     % width of moving window
14 - M9 = M8;
15 - for p=1:lengthcsv
16 -   for k=1:dimensionNew(p,1)
17 -     M9(k,[1:baseLine(k,1,p),end-m:end],p) = 0;
18 -   end
19 - end
20 - for p=1:lengthcsv
21 -   for k=1:dimensionNew(p,1)
22 -     for i=baseLine(k,1,p)-w:length(M9(k,:,p))-w
23 -       M10(k,i+w,p) = sum(M9(k,i:i+w,p))/w;
24 -     end
25 -   end
26 - end

```

## APPENDIX 9: Generating histograms from the results of the Trapezoidal filter algorithm

The image shows two MATLAB code snippets in the editor, each with a title bar 'Editor - histogramTRA.m' and a tab bar showing other open files: risingPart.m, decreasingPart.m, combineDeconv.m, combineDeconv2.m, histogramMWD.m, trapezoid.m, histogramTRA.m.

**Top Snippet (Lines 1-29):**

```

1 % % In this software section, the trapezoidal shape is worked on.
2 % % First of all, in this algorithm, the M11 matrix contains the
3 % % maximum data of the trapezoidal filter. That is, the higher
4 % % parts of the signals are averaged and recorded. Then all the
5 % % traces obtained are taken from all files and stored in the
6 % % MhistogramTra matrix. This matrix is where all the data comes
7 % % together to create a histogram. Histogram of Counts / Channel
8 % % type is created with MhistogramTra. Then, using the slope and
9 % % intercept of the linear equation produced for calibration,
10 % % the MEnergyTra matrix is created. This matrix is the matrix
11 % % where histogram information of type Counts / Energy is stored.
12
13 - trapezoid;
14 - for p=1:lengthcsv
15 -   for k=1:dimensionNew(p,1)
16 -     M11(k,1,p) = mean(M10(k,baseLine(k,1,p)+w+2:end-m-1,p));
17 -   end
18 - end
19
20 - MhistogramTra=[M11(1:dimensionNew(1,1),1,1);
21 - M11(1:dimensionNew(2,1),1,2);
22 - M11(1:dimensionNew(3,1),1,3);
23 - M11(1:dimensionNew(4,1),1,4);
24 - M11(1:dimensionNew(5,1),1,5);
25 - M11(1:dimensionNew(6,1),1,6);
26 - M11(1:dimensionNew(7,1),1,7);
27 - M11(1:dimensionNew(8,1),1,8);
28 - M11(1:dimensionNew(9,1),1,9);
29 - M11(1:dimensionNew(10,1),1,10);

```

**Bottom Snippet (Lines 22-44):**

```

22 M11(1:dimensionNew(3,1),1,3);
23 M11(1:dimensionNew(4,1),1,4);
24 M11(1:dimensionNew(5,1),1,5);
25 M11(1:dimensionNew(6,1),1,6);
26 M11(1:dimensionNew(7,1),1,7);
27 M11(1:dimensionNew(8,1),1,8);
28 M11(1:dimensionNew(9,1),1,9);
29 M11(1:dimensionNew(10,1),1,10);
30 M11(1:dimensionNew(11,1),1,11]);
31
32 figure(150);
33 hh = histogram(MhistogramTra(:,1),100);
34 title('TRAPEZOIDAL(MWD)'); xlabel('Channel'); ylabel('Counts');
35 hold on; grid on; grid minor;
36 edges = hh.BinEdges;
37 counts = hh.BinCounts;
38 values = hh.Values;
39 MEnergyTra(:,1) = 8.1818*MhistogramTra(:,1)+21.667;
40 figure(160); histogram(MEnergyTra(:,1),100);
41 title('TRAPEZOIDAL(MWD)'); xlabel('Energy(keV)'); ylabel('Counts');
42 hold on; grid on; grid minor; ax.MinorHistVvaluesGridLineStyle = '-.';


```

## APPENDIX 10: Algorithm that allows visualization of each signal processing step

```

Editor - figurePlot.m*
+7 | combineDeconv.m | combineDeconv2.m | histogramMWD.m | trapezoid.m | histogramTRA.m | figurePlot.m* | TOPLU_WORK1.m | + |
1 % % A step-by-step algorithm to see the state of any matrix,
2 % % any trace. A more detailed examination can be made by
3 % % removing the comment lines used in this algorithm and
4 % % plotting the desired matrix. Thanks to the "for" loop,
5 % % all data are plotted in a single window.
6
7
8 - for p=1:lengthcsv
9     % figure(1);
10    subplot(lengthcsv,1,p) %M1 plot
11    for k=1:dimension(p,1)
12        plot(1:500,M1(k,1:500,p)); hold on;
13        title('M1');
14        disp("M1 cizdirildi: " + k);
15    end
16
17    % figure(2);
18    subplot(lengthcsv,1,p) %M2 plot
19    for k=1:dimension(p,1)
20        plot(1:500,M2(k,1:500,p)); hold on;
21        title('M2');
22        disp("M2 cizdirildi: " + k);
23    end
24
25    % figure(3);
26    subplot(lengthcsv,1,p) %M3 plot
27    for k=1:dimension(p,1)
28        plot(1:500,M3(k,1:500,p)); hold on;
29        title('M3');
30        disp("M3 cizdirildi: " + k);
31
32
33    % figure(4);
34    subplot(lengthcsv,1,p) %M4 plot
35    for k=1:dimensionNew(p,1)
36
37        plot(1:500,M4(k,1:500,p)); hold on;
38        title('M4');
39        disp("M4 cizdirildi: " + k);
40    end
41
42    % figure(5);
43    subplot(lengthcsv,1,p) %M5 plot
44    for k=1:dimensionNew(p,1)
45        plot(1:500,M5(k,1:500,p)); hold on;
46        title('M5');
47        disp("M5 cizdirildi: " + k);
48    end
49
50    % figure(6);
51    subplot(lengthcsv,1,p) %M6 plot
52    for k=1:dimensionNew(p,1)
53        plot(1:500,M6(k,1:500,p)); hold on;
54        title('M6');
55        disp("M6 cizdirildi: " + k);
56    end
57
58    % figure(7);
59    subplot(lengthcsv,1,p) %M7 plot

```

```

Editor - figurePlot.m
+7 combineDeconv.m x combineDeconv2.m x histogramMWD.m x trapezoid.m x histogramTRA.m x figurePlot.m x TOPLU_WORK1.m x +
59 % subplot(lengthcsv,1,p) %M7 plot
60 % for k=1:dimensionNew(p,1)
61 % figure(p+10);
62 % plot(1:500,M7(k,1:500,p)); hold on;
63 % title('M7');
64 % disp("M7 cizdirildi: " + k);
65 %
66 %
67 % figure(8);
68 % subplot(lengthcsv,1,p) %M8 plot
69 % for k=1:dimensionNew(p,1)
70 % plot(1:450,M8(k,1:450,p)); hold on;
71 % title('M8');
72 % disp("M8 cizdirildi: " + k);
73 %
74 %
75 % figure(9);
76 % subplot(lengthcsv,1,p) %M9 plot
77 % for k=1:dimensionNew(p,1)
78 % plot(1:450,M9(k,1:450,p)); hold on;
79 % title('M9');
80 % disp("M9 cizdirildi: " + k);
81 %
82 %
83 %
84 % subplot(lengthcsv,1,p); %M10 plot
85 - for k=1:dimensionNew(p,1)
86 - figure(p+100);
87 - plot(2:450,M10(k,2:450,p)); hold on; grid on; grid minor;

```

```

Editor - figurePlot.m
+7 combineDeconv.m x combineDeconv2.m x histogramMWD.m x trapezoid.m x histogramTRA.m x figurePlot.m x TOPLU_WORK1.m x +
80 % disp("M9 cizdirildi: " + k);
81 %
82 %
83 %
84 % subplot(lengthcsv,1,p); %M10 plot
85 - for k=1:dimensionNew(p,1)
86 - figure(p+100);
87 - plot(2:450,M10(k,2:450,p)); hold on; grid on; grid minor;
88 - title('M10');
89 - disp("M10 cizdirildi: " + k);
90 %
91 %
92 %
93 % figure(100);
94 % subplot(lengthcsv,1,p); %M10 plot __ Trapezoid histogram part
95 % for k=1:dimensionNew(p,1)
96 % plot(M10(k,baseLine(k,1,p)+w+2:end-m-1,p)); hold on; grid on; grid minor;
97 % title('M10');
98 % disp("M10 cizdirildi: " + k);
99 %
100 %
101 % figure(100);
102 % subplot(lengthcsv,1,p); %M10 plot _ MWD % histogram part
103 % for k=1:dimensionNew(p,1)
104 % plot(M8(k,baseLine(k,1,p)+51:end,p)); hold on; grid on; grid minor;
105 % title('M10');
106 % disp("M10 cizdirildi: " + k);
107 %
108 %
109 - end

```

## REFERENCES

- [1] M. F. L'Annunziata, "Nuclear radiation, its interaction with matter and radioisotope decay," *Handb. Radioact. Anal.*, pp. 1–122, 2003.
- [2] G. F. Knoll, *Radiation detection and measurement*. John Wiley & Sons, 2010.
- [3] F. N. Flakus, "Detecting and Measuring Ionizing Radiation- A Short History.," *IAEA Bull.*, vol. 23, no. 4, pp. 31–36, 1982.
- [4] J. Y. Duboz, P. A. Badoz, F. A. d'Avitaya, and J. A. Chroboczek, "Electronic transport properties of epitaxial erbium silicide/silicon heterostructures," *Appl. Phys. Lett.*, vol. 55, no. 1, pp. 84–86, 1989.
- [5] P. Rajai, H. Ahmed, M. Straeten, G. Xereas, and M. J. Ahamed, "Analytical modeling of n-type doped silicon elastic constants and frequency-compensation of Lamé mode microresonators," *Sensors Actuators A Phys.*, vol. 297, p. 111508, 2019.
- [6] L. C. Linares and S. S. Li, "An Improved Model for Analyzing Hole Mobility and Resistivity in p-Type Silicon Doped with Boron, Gallium, and Indium," *J. Electrochem. Soc.*, vol. 128, no. 3, p. 601, 1981.
- [7] S. Tavernier, *Experimental techniques in nuclear and particle physics*. Springer Science & Business Media, 2010.
- [8] U. Forsberg, "Pulse Shape Analysis for Heavy Element Spectroscopy." Master's thesis, Division of Nuclear Physics, Lund University, 2010.
- [9] R. Page, "Radiometrics: Instrumentation and Modelling. Alpha Spectrometry Lecture Notes," the University of Liverpool, 2019.
- [10] Ortec, "Preamplifier Introduction," 2008. [Online]. Available: <https://www.ortec-online.com/-/media/ametekortec/other/preamplifier-introduction.pdf>.
- [11] Wikipedia, "Flash ADC." [https://en.wikipedia.org/wiki/Flash\\_ADC](https://en.wikipedia.org/wiki/Flash_ADC).
- [12] Micron Semiconductor, "Double Sided Silicon Strip Detector BB20." <http://www.micronsemiconductor.co.uk/product/bb20/>.
- [13] M. Nakhostin, *Signal processing for radiation detectors*. John Wiley & Sons, 2017.
- [14] MesyTec, "Nuclear Physics MPRT-16." [Online]. Available: <https://www.mesyttec.com/products/nuclear-physics/MPRT-16.html>.
- [15] N. Company, "VHS-ADC." <https://www.nutaq.com/sites/default/files/VHS-ADC.pdf>

ADC\_Scientific\_Nutaq\_LowRes.pdf.

- [16] M. Bogovac, D. Wegrzynek, and A. Markowicz, “Implementation of digital signal processor for nuclear spectrometry using state of the art tools,” *Signal Process. Electron. Nucl. Spectrom.*, vol. 20, p. 17, 2007.
- [17] V. T. Jordanov, G. F. Knoll, A. C. Huber, and J. A. Pantazis, “Digital techniques for real-time pulse shaping in radiation measurements,” *Nucl. Instruments Methods Phys. Res. Sect. A Accel. Spectrometers, Detect. Assoc. Equip.*, vol. 353, no. 1–3, pp. 261–264, 1994.
- [18] S. N. Bateman, A. Pejović-Milić, I. M. Stronach, F. E. McNeill, and D. R. Chettle, “Performance appraisals of digital spectroscopy systems for the measurement of bone lead,” *Appl. Radiat. Isot.*, vol. 53, no. 4–5, pp. 647–650, 2000.
- [19] C. A. McGrath and R. J. Gehrke, “A comparison of pulser-based analog and digital spectrometers,” *J. Radioanal. Nucl. Chem.*, vol. 276, no. 3, pp. 669–675, 2008.
- [20] D. T. Vo and P. A. Russo, “Comparisons of the portable digital spectrometer systems,” *Los Alamos Natl. Lab (LA-13895-MS, Issued Feb. 2002)*, 2002.
- [21] A. Georgiev, W. G.-I. T. on nuclear science, and undefined 1993, “Digital pulse processing in high resolution, high throughput, gamma-ray spectroscopy,” *ieeexplore.ieee.org*, Accessed: May 19, 2020. [Online]. Available: <https://ieeexplore.ieee.org/abstract/document/256659/>.
- [22] A. Georgiev, W. Gast, and R. M. Lieder, “An analog-to-digital conversion based on a moving window deconvolution,” *IEEE Trans. Nucl. Sci.*, vol. 41, no. 4, pp. 1116–1124, 1994.
- [23] J. Stein, F. Scheuer, W. Gast, and A. Georgiev, “X-ray detectors with digitized preamplifiers,” *Nucl. Instruments Methods Phys. Res. Sect. B Beam Interact. with Mater. Atoms*, vol. 113, no. 1–4, pp. 141–145, 1996, doi: 10.1016/0168-583X(95)01417-9.
- [24] V. T. Jordanov and G. F. Knoll, “Digital synthesis of pulse shapes in real time for high resolution radiation spectroscopy,” *Nucl. Instruments Methods Phys. Res. Sect. A Accel. Spectrometers, Detect. Assoc. Equip.*, vol. 345, no. 2, pp. 337–345, 1994.
- [25] T. Lakatos, J. Molnar, and E. Madarasz, “Signal processing method for nuclear spectrometers.” Google Patents, Apr. 02, 1991.
- [26] B. Hubbard-Nelson, M. Momayezi, and W. K. Warburton, “A module for energy and pulse shape data acquisition,” *Nucl. Instruments Methods Phys. Res. Sect. A Accel. Spectrometers, Detect. Assoc. Equip.*, vol. 422,

no. 1–3, pp. 411–416, 1999.

- [27] V. T. Jordanov, “Deconvolution of pulses from a detector-amplifier configuration,” *Nucl. Instruments Methods Phys. Res. Sect. A Accel. Spectrometers, Detect. Assoc. Equip.*, vol. 351, no. 2–3, pp. 592–594, 1994.
- [28] T. Kihm, V. F. Bobrakov, and H. V Klapdor-Kleingrothaus, “A digital multi-channel spectroscopy system with 100MHz flash ADC module for the GENIUS-TF and GENIUS projects,” *Nucl. Instruments Methods Phys. Res. Sect. A Accel. Spectrometers, Detect. Assoc. Equip.*, vol. 498, no. 1–3, pp. 334–339, 2003.
- [29] W. K. Warburton and Z. C. Zhou, “Method and apparatus for combinatorial logic signal processor in a digitally based high speed x-ray spectrometer.” Google Patents, Feb. 16, 1999.
- [30] A. Roth, “Extraction of energy and time from pile-up pulses with fast sampling ADC analysis techniques,” 2016.
- [31] P. Pusa, “Radiometrics: Instrumentation and Modelling. Simple Modelling Lecture Notes,” Liverpool.
- [32] L. H. Brennan, “Radiometrics: Instrumentation and Modelling. Nuclear Instrumentation Lecture Notes,” Liverpool.
- [33] Andrew Boston, “Radiometrics: Instrumentation and Modelling. Statictics Lecture Notes,” Liverpool.
- [34] P. A. Miranda, U. Wahl, N. Catarino, M. R. da Silva, and E. Alves, “Performance of resistive-charge position sensitive detectors for RBS/Channeling applications,” *Nucl. Instruments Methods Phys. Res. Sect. A Accel. Spectrometers, Detect. Assoc. Equip.*, vol. 760, pp. 98–106, 2014.